2020 Nunavut Research Licence Renewal Application: Wayne Pollard

Project Title: An investigation of the sensitivity of high Arctic permafrost to climate change

Principal investigator: Dr. Wayne Pollard, Professor, Department of Geography, McGill University, 805 Sherbrooke St. W. Montreal, Quebec. H3A 0B9

2020 Research Team: Wayne Pollard (PI), Chris Omelon (Co-PI), Dale Andersen, Denis Lacelle, Anthony Zerafa (Ph.D.), Frances Amyot (M.Sc.) and 1 new MSc student – This is a university-based research project.

2020 Fieldwork Schedule: Planned fieldwork April 1- August 30.

2020 Field sites: The Expedition Fiord area on Axel Heiberg Island (79º25'N; 90º45'W) and the Eureka area on the Fosheim Peninsula, Ellesmere Island (80º00'N 85º95'W). We will be based at the McGill station on Axel Heiberg Island and the Eureka Weather Station.

Funding source: Discovery Grant from the Natural Science and Engineering Research Council (NSERC). Logistical support is provided by the Polar Continental Shelf Program

Project Overview:

I am in the process of winding down a long-term project examining how global warming linked to warmer summer temperatures, is effecting the stability of high Arctic permafrost conditions, landscapes and infrastructure. The timeline for this corresponds the current cycle of my NSERC funding awarded for this research. My long-term project aims have been as follows: (1) to identify and measure changes (and rates of change) occurring in tundra and polar desert landscapes related to increased active layer thickness and thermokarst, (2) to determine ground ice and permafrost characteristics and assess their vulnerability to climate change, and (3) to assess local climate variability. Linked to these aims has also been the development of non-invasive shallow geophysical techniques, dGPS and UAVs as tools to detect and monitor changing permafrost conditions. The importance of this research is highlighted by the dramatic increase in thawing permafrost observed in the unusually warm summers in 2011 and 2012. The information collected in this study will improve our understanding of how climate and permafrost interact, and the potential resiliency of permafrost systems to changing summer conditions, both of which will allow for the better prediction of future changes. This research also has a significant training component involving students on several levels.

Progress Report – 2019 Scientific Research Licence #02 027 19R-M (multiyear)

In 2019 fieldwork continued in the Eureka Sound area on Ellesmere Island and Expedition Fiord area on Axel Heiberg Island. My research team was based at the Eureka weather station for most of July during which we repeated on going measurements of thaw slump retreat and ice wedge subsidence around the Environment Canada weather station, runway and DND base. Fieldwork at Expedition Fiord area of Axel Heiberg Island occurred during the first part of July. At Eureka work included dGPS, GPR and vegetation surveys in areas where thermokarst and erosion appear to be increasing (PhD. Research of M. Ward, MSc. Research of K. Campbell-Heaton). Ice and soil samples were collected for chemical, organic carbon and ice content analyses. Results to date are interesting, we found that Total Soil Carbon (TSC) contents in the active layer for most of the area are extremely variable and seem to increase with depth. TSC in wetlands is much higher (2-5%) as expected. Since wetlands cover less than 3 % of the land area they represent a small potential carbon source. In 2019 the trend in active layer development and thermokarst was consistent with fairly typical summer conditions (Ward PhD). The Eureka area contains extensive massive ground ice deposits (massive ground ice refers to thick (3-10m) layers of nearly pure ice) beneath 1-4 m of marine sediments. The presence of massive ice makes this area extremely vulnerable to thaw subsidence and erosion. My work in the Eureka Sound Lowlands over the past 2 decades has identified a series of "hotspots" where ground ice represents a significant part of the near surface permafrost. Since 2011 we have mapped thaw and changing landscape conditions related to ground ice almost everywhere below 150m asl. In 2012 we reported an unprecedented level of thermokarst (250+ retrogressive thaw slumps) but in 2019 (like 2018) the pattern of thermokarst was marked by low levels of activity. MSc student F. Amyot continued her research on the detection of unstable terrain using a UAV and GPR. Ongoing aerial surveys and monitoring of retrogressive thaw slump activity is part of the PhD research by M. Ward. In addition to field mapping areas of thermokarst Ward is using satellite imagery to map and monitor landscape scale changes. Other fieldwork included ground penetrating radar surveys of ice wedges and massive ice deposits, sampling of ground ice and aerial surveys. Appendix 1 provides results from an ongoing study of ice chemistry.

2020 Field Program.

This project is entering its final stage winding up 2020. The aim of my 2020 field program is to complete investigations concerned with the nature and distribution of ice-rich permafrost and in particular its vulnerability and thermokarst processes. My 2020 field program will address focus on: (1) changes in the active layer depth and its impact on surface topography, (2) changes in ice wedge morphology and (3) analysis of the chemistry of massive ground ice and ice wedge ice. The latter collaborative work with D. Lacelle and his graduate students. The measurement of changes occurring in the active layer remains a key focus as well as identifying connections between the atmosphere, active layer and permafrost. Fieldwork is planned for the Expedition Fiord area on Axel Heiberg Island (79º25N; 90º43'W) and the Eureka area on Ellesmere Island (79º59'N; 85º49'W). Our sites were selected in 2012 and are representative of the most common ecosystems in this part of the Arctic. These sites were chosen because of their accessibility, availability of baseline data, and existing research facilities. This research will assess the sensitivity of key permafrost systems to warming by defining how surface temperature fluctuations influence the depth of the active layer and changes at the active layer permafrost interface. In this study we hope to identify critical thresholds of non-recoverable change known as tipping points, and potential feedbacks (main focus of my NSERC grant). In 2020 I am asking 2 key questions that carry over from 2019: (1) does the active layer buffer the permafrost system? And, (2) do ice wedge polygons respond differently than other permafrost systems? Activities planned for 2020 include the measurement of changes in the ground surface using a high resolution gps system coupled with ground penetrating radar. These data will be included in a geographic information system and will be used to geo-reference satellite images, (b) monitoring active layer processes and the measurement of temperature and moisture changes in mid-summer. This will involve the collection of sediment and ice samples from the active layer and top of permafrost, and (c) continued aerial surveys of changes throughout the Fosheim Peninsula. A component unsuccessful in 2018 & 2019 was the utilization of a UAV to map spatial patterns of small scale surface change as well as thermokarst. We have updated the firmware on our UAV which hopefully has solved our problem.

Significance:

This research is making a significant contribution to the understanding of permafrost and ground ice conditions in the high Arctic. It has contributed new insights into the origin and age of permafrost systems, rates of change and the potential vulnerability of ice cored landforms and ice wedge polygons. The magnitude of warming projected for the high Arctic will have significant effects on both the ecology and geomorphology of the region. This work is even more important given the increased level of mineral exploration interests in this area. I have attached a copy of a recent report concerned with the evolution of massive ice on the Fosheim Peninsula.

Wayne Pollard, Professor
McGill University

2020 ᓄᓇᕗᒥ ᖃᐅᔨᓴᕐᓂᕐᒧᑦ ᐱᔪᓐᓇᐅᑎᖓᓂ ᓄᑖᙳᕆᐊᕈᒪᓂᖅ ᐱᓇᓱᒍᑎ: ᕗᐊᐃᓐ ᐳᓪᓚᕐᑦ

<u>ᐱᓕᕆᐊᖑᑕ ᑕᐃᔭᐅᓂᖓ: ᖃᐅᔨᓴᕐᓂᖅ ᐃᒃᐱᒃᓇᕐᑎᒋᖃᑦᑕᕐᓂᖓᓂᒃ ᖁᑦᑎᒃᑐᒥ ᓄᓇᐅᑦ ᖁᐊᖑᓂᖓ ᓯᓚᒧᑦ ᐊᓯᓪᓕᕐᐸᓪᓕᐊᔪᒧᑦ</u>

ᐊᖓᔪᖅᑳᖅ ᖃᐅᔨᓴᕐᑎ: ᒨᒃᑖᖅ ᕗᐊᐃᓐ ᐳᓪᓚᕐᑦ, ᐃᓕᓴᐃᔨᒻᒪᕆᒃ, ᓄᓇᓕᕆᓂᕐᒧᑦ, ᒪᒃᒋᐅ ᐃᓕᓐᓂᐊᕐᕕᒃᔪᐊᖅ, 805 Sherbrooke St. W. Montreal, Quebec. H3A 0B9

2020 ᖃᐅᔨᓴᕐᑎᐅᔪᑦ: ᕗᐊᐃᓐ ᐳᓪᓚᕐᑦ (ᐊᖓᔪᖄᖅ), ᑯᕆᔅ ᐅᓕᓚᓐ, (ᑐᖏᓕᐊ ᐊᖓᔪᖄᖅ), ᑕᐃᐅᓪ ᓚᓯᐅᓪ, ᐊᓐᑕᓂ ᔨᕋᕙ (ᐃᓕᓐᓂᐊᕐᑎ), ᕗᕋᓐᓯᔅ ᐊᒥᐊᕐ(ᐃᓕᓐᓂᐊᕐᑎ) ᐊᒻᒪᓗ ᐊᑕᐅᓯᖅ ᓄᑖᙳᔪᖅ ᐃᓕᓐᓂᐊᕐᑎ- ᑖᓐᓇ ᐃᓕᓐᓂᐊᕐᕕᒃᔪᐊᕐᒥ ᖃᐅᔨᓴᕐᓂᐅᔪᖅ ᐱᓕᕆᐊᒃᓴᐅᔪᖅ.

2020 ᖃᐅᔨᓴᕐᓂᖏᑦ ᐅᓪᓗᖏᑦ: ᐸᕐᓇᐅᑕᐅᔪᖅ ᖃᐅᔨᓴᕐᓂᖓ ᐊᐃᕖᓪ 1 - ᐋᒌᓯ 30.

2020 ᖃᐅᔨᓴᕐᑎᓪᓗᒋᑦ ᐃᓂᖓ: ᑲᖏᕐᔫᐊᓂ Expedition Fiord ᓄᓇᖓᓂ ᕿᑭᕐᑕᐅᑉ Axel Heiberg Island (79º25’N; 90º45’W) ᐊᒻᒪᓗ ᐃᐅᓖᑲ ᓄᓇᖓᓂ ᐃᓚᖓᓂ Fosheim Peninsula, ᕿᑭᕐᑕᖓᓂ Ellesmere Island (80º00’N 85º95’W). ᐃᓂᖅᑲᕐᓂᐊᕐᑐᒍᑦ ᒪᒃᒋᐅ ᐃᒃᓗᕐᑯᑎᖓᓂ ᕿᑭᕐᑕᖓᓂ Axel Heiberg Island ᐊᒻᒪᓗ ᐃᐅᓖᑲ ᑎᓇᓐᓂᐊᕐᕕᒥ.

ᑮᓇᐅᔭᖅᑲᖅᕕᐅᔪᑦ: ᕿᓂᕐᓂᕐᒧᑦ ᑮᓇᐅᔭᕐᑖᙳᖅᑲᑦᑕᕐᑐᑦ ᓄᓇᒥ ᑭᒃᑲᓯᓂᐊᕐᓂᕐᒧᑦ ᐊᒻᒪᓗ ᐃᓗᓕᖏᓐᓂᒃ ᖃᐅᔨᓴᕐᓂᕐᒧᑦ ᑲᑎᒪᔨᖏᑦ (NSERC). ᐊᐅᓚᓂᖓᓄᑦ ᐃᑲᔪᕐᑐᐃᔪᑦ Polar Continental Shelf Program

ᐱᓕᕆᐊᒃᓴᒧᑦ ᑕᑯᓕᒫᕐᓗᒍ:

ᐋᕿᒃᓱᐃᕙᓪᓕᐊᓪᓗᖓ ᐃᓱᓕᑉᐸᓪᓕᐊᓕᖓᓄᑦ ᐊᑯᓂᐅᔪᒧᑦ ᐱᓕᕆᐊᒃᓴᐅᔪᖅ ᖃᐅᔾᓇᓱᒃᑐᑦ ᓄᓇᕐᔪᐊᕐᒥ ᐅᖁᓱᕙᓪᓕᐊᓂᖓᓄᑦ ᐊᒃᑐᐊᓂᖅᑲᕐᒪᖔᑦ ᐊᐅᔭᒃᑯᑦ ᐅᖁᓂᕐᓴᐅᖅᑲᑦᑕᓕᕐᓂᖓ, ᐃᒃᐱᖕᓇᐅᑎᖓᒪᖔᑦ ᖁᑦᑎᒃᑐᒥ ᓄᓇᐅᑦ ᖁᐊᖑᓂᖓ ᐊᐅᒃᐸᓪᓕᐊᖓᒪᖔᑦ, ᓄᓇᖓᓗ ᐊᒻᒪᓗ ᐱᖁᑎᓄᑦ ᓴᓇᓯᒪᔪᓄᑦ. ᖃᖓᒃᑰᖓᓂᖓ ᐅᓪᓗᖏᑦ ᒪᓕᒃᓯᒪᔪᖅ ᑮᓇᐅᔭᕐᑖᕈᑕᐅᓂᖓᓄᑦ NSERC ᖃᐅᔨᓴᕐᓂᕐᒧᑦ. ᐊᑯᓂᐅᔪᒧᑦ ᖃᐅᔨᓴᕐᓂᐅᔪᖅ ᑐᕋᖅᑲᖅᑐᖅ ᐅᑯᓂᖓ: (1) ᓇᓗᓇᐱᕐᓗᒋᑦ ᐊᒻᒪᓗ ᐆᒃᑐᕐᓗᒋᑦ ᐊᓯᓪᓕᕐᐸᓪᓕᐊᔪᑦ (ᐊᒻᒪᓗ ᖃᓄᑎᒋ ᓱᒃᑲᑎᒋᓂᖏᑦ ᐊᓯᓪᓕᕐᐸᓪᓕᐊᔪᑦ) ᓄᓇᖓᓂ ᓇᑎᕐᓇᒥ ᐊᒻᒪᓗ ᐸᓂᕐᑐᒥ ᓄᓇᖓᓂ ᐊᒃᑐᐊᓂᕆᔭᖓ ᐱᕙᓪᓕᐊᓂᖓ ᓄᓇᐅᑦ ᖄᖓ ᐊᐅᓚᓂᖓ ᐃᔾᔪᕐᑎᑉᐸᓪᓕᐊᓪᓗᓂ ᐊᒻᒪᓗ ᐊᐅᒃᐸᓪᓕᐊᓂᖓ, (2) ᖃᐅᔾᓇᓱᒃᓗᒍ ᓄᓇᒦᑦᑐᑦ ᓂᓚᐅᓂᖓ ᖁᐊᖑᓂᖓᓗ ᐃᓗᓕᖏᑦ ᐊᒻᒪᓗ ᑐᑭᓯᓇᓱᒃᓗᒋᑦ ᓯᓚᒧᑦ ᐊᓯᓪᓕᕐᐸᓪᓕᐊᓂᕐᒧᑦ ᐃᒃᐱᖕᓇᐅᑎᖅᑲᕐᒪᖔᑕ, ᐊᒻᒪᓗ (3) ᖃᐅᔨᓴᕐᓗᒍ ᓄᓇᖓ ᓯᓚᖓ ᐊᔾᔨᒌᖏᓕᕐᑕᖅᑲᑦᑕᕐᓂᖓ. ᐊᒃᑐᐊᓂᖓ ᑖᒃᑯᕗᖓ ᑐᕌᒐᐅᔪᓄᑦ ᐋᕿᒃᓱᐃᕙᓪᓕᐊᔪᒧᑦ ᐊᑐᕐᑕᐅᓂᐊᕐᑐᓂᒃ ᖃᐅᔨᓴᕈᑎᓂᒃ ᓄᓇᓕᕆᔾᔪᑎᓂᒃ ᒪᐅᖓᑦᑎᐊᖅ ᐊᒻᒪᓗ ᐃᒃᐱᓇᐅᑎᖃᖏᑦᑐᑦ ᐊᓯᖏᓐᓄᑦ ᐅᑯᐊ dGPS ᐊᒻᒪᓗ UAVs ᖃᐅᔨᓴᕈᑕᐅᓂᐊᕐᓗᑎᒃ ᐊᓯᓪᓕᕐᐸᓪᓕᐊᓂᖓᓂᒃ ᓄᓇᐅᑦ ᖁᐊᖑᓂᖓᓂᒃ ᖃᓄᐃᓕᐅᕙᓪᓕᐊᓂᖓᓂᒃ. ᐱᓪᒪᕆᐅᔾᔪᑎᒋᔭᖓ ᖃᐅᔨᓴᕐᓂᐅᑦ ᑐᑭᓯᔭᐅᔪᒪᓕᓗᓂ ᓱᒃᑲᔪᒥᒃ ᐊᐅᒃᐸᓪᓕᐊᓂᖓ ᓄᓇᐅᑦ ᖁᐊᖑᓂᖓ ᑕᑯᔭᐅᓯᒪᔪᖅ ᐅᖁᓂᖅᓴᐅᓕᖅᖓ ᐊᐅᔭᒃᑯᑦ 2011 ᐊᒻᒪᓗ 2012. ᖃᐅᔨᓴᕐᑕᐅᔪᑦ ᑎᑎᕋᕐᑕᐅᔪᑦ ᑐᑭᓰᓪᓕᕈᑕᐅᓂᐊᕐᒪᑕ ᖃᓄᖅ ᓯᓚ ᓄᓇᐅᓪᓗ ᖁᐊᖑᓂᖓ ᐊᒃᑐᐊᓂᖅᑲᕐᑎᒋᓂᖏᓐᓂᒃ, ᐊᒻᒪᓗ ᓱᕋᖏᑎᒋᔪᓐᓇᕐᓂᖓ ᓄᓇᐅᑦ ᖁᐊᖑᓂᖓ ᐊᓯᓪᓕᕐᐸᓪᓕᐊᑎᓪᓗᒍ ᐊᐅᔭᒃᑯᑦ ᐅᖁᓱᕙᓪᓕᐊᑎᓪᓗᒍ, ᓯᕗᓂᒃᓴᒧᑦ ᖃᓄᐃᓕᕆᔭᕐᓂᖓᓄᑦ ᑐᑭᓯᐅᒪᔾᔪᑕᐅᓂᐊᕐᒪᑦ. ᑖᓐᓇ ᖃᐅᔨᓴᕐᓂᖅ ᐃᓕᓐᓂᐊᕐᑎᑦᑎᓂᖅᑲᕐᓂᐊᕐᒥᔪᖅ ᐃᓕᓐᓂᐊᕐᑎᓂᒃ ᐊᔾᔨᒋᖏᑦᑐᓂᒃ ᖁᑦᑎᓕᕖᓂᒃ.

ᖃᓄᐃᓕᕙᓪᓕᐊᓂᖓᑕ ᐅᓂᒃᑲᖏᑦ - 2019 ᑭᒃᑲᓯᓂᐊᕐᓂᕐᒧᑦ ᖃᐅᔨᓴᕐᓂᕐᒧᑦ ᐱᔪᓐᓇᐅᑖ #02 027 19R-M (ᐊᕋᒍᖓᓴᒃᓄᑦ)

ᐊᕋᒍᖓᓂ 2019 ᖃᐅᔨᓴᕐᓂᖅ ᑲᔪᓯᓚᐅᕐᑐᖅ ᐃᐅᓕᑲ ᑲᖏᕐᓗᐊᓂ ᓄᓇᖓᓂ ᕿᑭᕐᑕᒥ Ellesmere Island ᐊᒻᒪᓗ ᑲᖏᕐᓗᐊᑕ ᓄᓇᖓᓂ Expedition Fiord ᓄᓇᖓᓂ ᕿᑭᕐᑕᐅᑉ Axel Heiberg Island. ᖃᐅᔨᓴᕐᑎᐅᔪᑦ ᑕᖕᒫᕐᓯᒪᖃᑦᑕᓚᐅᕐᑐᑦ ᐃᐅᓕᑲ ᓯᓚᓪᓕᐊᕙᖕᒥ ᔪᓚᐃᒥ ᐆᒃᑐᑯᑕᒃᓗᑎᒍ ᐊᐅᒃᐸᓪᓕᐊᑎᒋᓂᖓ ᖃᑦᑎᒃᓯᓕᕐᓯᒪᔪᖅ ᓄᓇᒥ ᐊᒻᒪᓗ ᓂᓚᐅᑦ ᓴᕿᐸᓪᓕᐊᔪᑦ ᐊᕙᑖᓂ ᓯᓚᓐᓂᐊᕐᕕᐅᑦ ᑲᓇᑕ, ᒥᑦᑕᕐᕕᒃᒥ ᐊᒻᒪᓗ ᐅᓇᑕᕐᑐᒃᓴᖃᕐᕕᖕᒥ. ᖃᐅᔨᓴᕐᓂᐅᔪᖅ ᑲᖏᕐᓗᐊᑕ ᓄᓇᖓᓂ ᕿᑭᕐᑕᒥ Expedition Fiord ᓄᓇᖓᓂ ᕿᑭᕐᑕᐅᑉ Axel Heiberg Island ᐊᑐᕐᑕᐅᓚᐅᕐᑐᖅ ᐃᓚᖓᓂ ᔫᓚᐃ. ᐃᐅᓕᑲᒥ ᖃᐅᔨᓴᕐᓂᖅ ᐅᑯᐊ ᐊᑐᕐᑕᐅᓚᐅᕐᑐᑦ dGPS, GPR ᐊᒻᒪᓗ ᐱᕈᕐᑐᓂᒃ ᖃᐅᔨᓴᕐᓂᖅ ᐊᐅᒃᐸᓪᓕᐊᓂᖓᓂᑦ ᓄᖑᑉᐸᓪᓕᐊᓪᓗᓂᓗ (ᐃᓕᓐᓂᐊᕐᑎ ᖃᐅᔨᓴᕐᓂᕐᒧᑦ L. ᐧᕗᐊᑦ M. Ward, ᐃᓕᓐᓂᐊᕐᑎᑦ ᖃᐅᔨᓴᕐᓂᕐᒧᑦ K. Campbell-Heaton). ᓂᓚᒃ ᐊᒻᒪᓗ ᐃᔾᔪᖅ ᖃᐅᔨᓴᖓᒃᓴᐃᑦ ᐱᕚᐅᖃᑦᑕᓚᐅᕐᑐᑦ ᐃᓗᓕᖏᓐᓂᒃ, ᐊᓐᓇᐅᒫᔾᔪᑎᖏᓪᓗ ᐊᒻᒪᓗ ᓂᓚᖃᕐᑎᒋᓂᖓᓂᒃ ᖃᐅᔨᓴᕐᑕᐅᓇᓱᒃᓗᑎᒃ. ᖃᐅᔨᓴᕈᑎᑦ ᒫᓐᓇᒧᑦ ᑐᓴᕈᒥᓇᓚᐅᕐᑐᑦ, ᖃᐅᔨᓚᐅᕐᑐᒍᑦ ᑲᑎᓪᓗᒋᑦ ᐃᔾᔪᐃᑦ ᓱᕈᕐᓇᕐᑐᕐᑲᕐᑎᒋᓂᖓ (TSC) ᐃᓗᓕᖏᑦ ᐊᐅᓚᓂᖓᑕ ᓄᓇᐅᑦ ᐊᔾᔨᖏᑦᑑᑕᐅᓚᐅᕐᑐᑦ ᐱᓂᖃᐅᕚᓪᓕᐊᓪᓗᓂᓗ ᑕᐅᓅᖓᐅᕚᓪᓕᐊᓪᓗᓂ. ᑲᑎᓪᓗᒋᑦ ᐃᔾᔪᐃᑦ ᓱᕈᕐᓇᕐᑐᕐᑲᕐᑎᒋᓂᖓ TSC ᐃᒪᕐᓱᖏᓐᓂ ᖁᑦᑎᒃᓂᖃᐅᓚᐅᕐᑐᖅ (2-5%) ᓂᕆᐅᒋᕚᐅᓚᐅᕐᓗᓂᓗ. ᐃᒪᕐᓱᐃᑦ ᒥᑭᓐᓂᖃᐅᓂᖏᓐᓄᑦ ᓄᓇᖓᓃᑦᑐᑦ ᐃᒪᓐᓇᑎᒋ 3 % ᒥᑭᑦᑐᒥᒃ ᓱᕈᕐᓇᕐᑐᑦ ᓴᕿᐸᓪᓕᐊᔪᑕᐅᓴᕐᓂᖓᓂᒃ. ᐊᕋᒍᖓᓂ 2019 ᖃᓄᐃᓕᕚᓪᓕᐊᓂᖓ ᓄᓇᐅᑦ ᐊᐅᓚᓂᖓ ᐱᕚᓪᓕᐊᓂᖓ ᐊᒻᒪᓗ ᐊᐅᓚᓂᖓ ᑕᐃᒪᓐᓇᑦᑕᐃᓐᓇᐅᓚᐅᕐᑐᖅ ᐊᐅᓭᖓᓗ ᐃᓕᕐᑯᓯᕐᓱᕐᓗᓂ (Ward PhD). ᐅᐃᓕᑲ ᓄᓇᖓᓂ ᓂᓚᖃᐅᕐᒪᑦ (ᐊᖏᔫᑎᑦ ᓄᓇᒥ ᓂᓚᐃᑦ ᐃᔾᔪᓂᖃᕐᑐᖅ (3-10ᒦC) ᓂᓚᑐᐃᓐᓇᐅᓪᓗᓂ) ᐊᑖᓂ 1-4 ᒦC ᐃᖃᕙᓂᐅᓪᓗᓂ ᑕᕆᐅᕐᒥ. ᐱᑕᖃᕐᓂᖓ ᓂᓚᒃᒥᒃ ᐊᖏᔪᒥ ᑖᓐᓇ ᓄᓇ ᐊᐅᒃᐸᓪᓕᐊᓂᖕᓴᐅᑐᐃᓐᓇᕆᐊᓕᒃ ᓄᖑᐸᓪᓕᐊᔪᒧᓪᓗ. ᖃᐅᔨᓴᕐᓂᕆᓴᕗᑦ ᐃᐅᓕᑲ ᓄᓇᖓᓂ Hᑎᕐᓇᖓᓂ ᐊᕋᒍᓄᑦ 20-ᓄᑦ ᓇᓗᓇᐃᕐᓯᓯᒪᔪᑦ ᐅᓄᕐᑐᑦ “ᐅᖅᑰᓂᖏᑦ: ᓄᓇᒥ ᓂᓚᖃᕐᓂᖅᓴᐅᓪᓗᓂ ᓄᓇᐅ ᖃᖓᓃᑦᑐᒧᑦ ᖁᐊᖑᓂᖓᓄᑦ. ᑕᐃᒪᖓᑦ 2011 ᓄᓇᖑᐊᓕᐅᕐᓯᒪᔪᒍᑦ ᐊᐅᒃᐸᓪᓕᐊᓂᖓᓂᒃ ᐊᒻᒪᓗ ᐊᓯᓪᓕᕐᐸᓪᓕᐊᓂᖓᓂᒃ ᓄᓇᐅᑉ ᓂᓚᒃᒧᑦ ᓄᓇᒥᑦ ᑎᑭᓗᒍ ᑕᐅᓄᖓ 150ᒦC asl. ᐊᕋᒍᖓᓂ 2012 ᐅᖃᐅᓯᖃᓚᐅᕋᑦᑕ ᐊᔾᔨᐅᖏᑦᑑᓂᖓᓂᒃ ᐊᐅᒪᓂᖓ (250+ ᐊᐅᒃᐸᓪᓕᐊᓂᖓᓄᑦ ᖃᑦᑎᒃᓯᕙᓪᓕᐊᔪᑦ) ᑭᓯᐊᓂ 2019 (ᑕᐃᒪᓐᓇᑦᑕᐅᖅ 2018) ᐊᐅᒃᐸᓪᓕᐊᑎᒋᓂᖓ ᓱᕋᖏᓐᓂᖅᓴᐅᓚᐅᕐᑐᖅ. ᐃᓕᓐᓂᐊᕐᑎ F. Amyot ᐊᒧᐊᐃᑦ ᖃᐅᔨᓴᕐᐸᓪᓕᐊᖏᓐᓇᕐᑐᖅ ᖃᐅᔨᓴᕈᑎᓂᒃ ᐊᑐᕐᓗᓂ ᓄᓇᖓᓂ. ᖃᖓᑕᕋᕈᑎᒧᓪᓗ ᖃᐅᔨᓴᕐᑕᐅᕙᓪᓕᐊᔪᑦ ᐊᐅᒃᐸᓪᓕᐊᓂᖓ ᖃᑦᑎᒃᓯᓕᕐᓯᒪᔪᑦ ᐃᓚᒋᔭᖓ ᐃᓕᓐᓂᐊᕈᑎᖓᓄᑦ ᖃᐅᔨᓴᕐᓂᕐᒧᑦ ᐃᓕᓐᓂᐊᕐᑎ L. ᐧᕗᐊᑦᔭ ᐊᒻᒪᓗ ᓄᓇᖑᐊᓕᐅᕐᑕᐅᕙᓪᓕᐊᓪᓗᓂ ᐊᐅᒃᐸᓪᓕᐊᓂᖓ ᐧᕗᐊᑦ ᐊᑐᖃᑦᑕᕐᒥᔪᖅ ᖃᖓᑦᑕᕐᑎᑕᐅᓯᒪᔫᒃᑯᑦ ᐊᔾᔨᖑᐊᓂᒃ ᓇᓗᓇᐃᕐᐸᓪᓕᐊᓪᓗᒋᑦ ᖃᐅᔨᓴᕈᑎᒋᓗᒋᓪᓗ ᐊᓯᓪᓕᕐᐸᓪᓕᐊᓂᐅᔪᑦ. ᐊᓯᖏᑦ ᖃᐅᔨᓴᕐᓂᐅᔪᑦ ᐱᖃᓯᐅᑎᓪᓗᒋᑦ ᓄᓇᒥ ᖃᐅᔨᓴᕈᑎᑦ ᓂᓚᐅᓂᖏᓐᓂᒃ ᐊᒻᒪᓗ ᐊᖏᓂᖓ ᓂᓚᐅᑉ, ᖃᐅᔨᓴᕐᑕᐅᓗᓂᓗ ᓄᓇᒦᖓᕐᑐᑦ ᓂᓚᐃᑦ ᐊᒻᒪᓗ ᖃᖓᑕᕋᕐᓂᒃᑯᑦ ᐊᔾᔨᓕᐅᖓᐃᑦ.

2020 ᖃᐅᔨᓴᕐᓂᖅ ᐊᐅᓚᓂᖓ.

ᑖᓐᓇ ᐱᓕᕆᐊᒃᓴᐅᔪᖅ ᑭᖑᓪᓕᕐᐹᕐᓂᐊᓕᕐᑐᖅ ᐊᕋᒍᒧᑦ 2020. ᑐᕌᖓᐅᔪᑦ 2020-ᒥ ᐱᔭᕇᕐᑕᐅᓗᑎᒃ ᖃᐅᔨᓴᕐᓂᐅᔪᑦ ᓂᓚᖃᕐᓂᖏᑦ ᓄᓇᐅᑦ ᖁᐊᖑᓂᖓ ᐊᒻᒪᓗ ᐱᓗᐊᕐᑐᒥᒃ ᐃᒃᐱᖓᐅᑎᒋᓂᖓ ᐊᒻᒪᓗ ᐊᐅᒃᐸᓪᓕᐊᑎᒋᓂᖓ. ᐊᕋᒍᖓᓂ 2020 ᖃᐅᔨᓴᕐᓂᐅᔪᖅ ᐅᑯᓂᖓ ᐱᓇᓱᒃᓂᐊᕐᑐᑦ: (1) ᐊᓯᓪᓕᕐᐸᓪᓕᐊᔪᑦ ᓄᓇᐅᑦ ᐊᐅᒪᓂᖓ ᐊᒻᒪᓗ ᐃᒃᐱᖓᐅᑎᓂᖓ ᓄᓇᖓᓄᑦ ᐋᕿᒃᓯᒪᓂᖓᓄᑦ, (2) ᐊᓯᓪᓕᕐᐸᓪᓕᐊᓂᐅᔪᑦ ᓂᓚᐅᓂᖓ ᐋᕿᒃᓯᒪᓂᖓ ᐊᒻᒪᓗ (3) ᖃᐅᔨᓴᕐᓂᖅ ᐃᓗᓕᖏᓐᓂᒃ ᐊᖏᔪᑎᑦ ᓂᓚᐅᓂᖓ ᓄᓇᒥᑦ ᐊᒻᒪᓗ ᖃᑦᑎᒃᓂᐅᔪᑦ ᓂᓚᐃᑦ. ᖃᐅᔨᓴᕐᓂᐅᓂᐊᕐᑐᖅ ᑎᔭ ᓚᓯᐅᓪ ᐃᓕᓐᓂᐊᕐᑎᓂᒃᓗ. ᐆᑐᕋᕐᑕᐅᓗᑎᒃ ᐊᓯᓪᓕᕐᐸᓪᓕᐊᔪᑦ ᓄᓇᐅᑦ ᖄᖓᓂ ᑐᕋᓚᕆᔭᐅᓪᓗᐊᑕᕐᓂᐊᕐᑐᖅ ᐊᒻᒪᓗ ᓇᓗᓇᐃᕐᑕᐅᓂᖏᑦ ᐊᒃᑐᐊᓂᕆᔭᖏᑦ ᓯᓚᐅᑦ, ᓄᓇᐅᑦ ᐊᐅᒪᓂᖓ ᐊᒻᒪᓗ ᖁᐊᖑᓂᖓ. ᖃᐅᔨᓴᕐᓂᐅᔪᖅ ᐸᕐᓇᐅᑎᒋᔭᕗᑦ ᑲᖏᕐᓗᐊᑕ ᓄᓇᖓᓂ ᕿᑭᕐᑕᒥ Expedition Fiord ᓄᓇᖓᓂ ᕿᑭᕐᑕᐅᑉ Axel Heiberg Island (79º25N; 90º43’W) ᐊᒻᒪᓗ ᐃᐅᓕᑲ ᓄᓇᖓᓂ ᕿᑭᕐᑕᒥ Ellesmere Island (79º59’N; 85º49’W). ᓂᕈᐊᕐᑕᐅᓚᐅᕐᑑᒃ ᓄᓇᐃᑦ ᖃᐅᔨᓴᕐᕕᐅᔪᒪᓪᓗᑎᒃ ᐊᕋᒍᖓᓂ 2012 ᐊᔾᔨᒋᔭᖃᕐᓂᖏᓐᓂᒃ ᓄᓇᖓᓂᓕᒫᖅ ᐅᑭᐅᕐᑕᕐᑐᒥ. ᑖᑯᐊ ᓄᓇᐃᑦ ᓄᕈᐊᕐᑕᐅᓚᐅᕐᑑᒃ ᐱᔾᔪᑎᒋᓪᓗᒍ

ᐅᐸᒐᒃᓴᐅᓂᖏᓐᓄᑦ ᐊᒻᒪᓗ ᖃᐅᔨᓴᕐᑕᐅᖃᑦᑕᕐᓯᒪᓂᖏᓐᓄᑦ, ᐊᒻᒪ ᖃᐅᔨᓴᕐᕙᒃᑕᖃᕐᓂᖕᓄᑦ. ᑖᓐᓇ ᖃᐅᔨᓴᕐᓂᖅ ᑐᑭᓯᓇᓱᖕᓂᐊᕐᒪᑦ ᐃᒃᐱᖕᓇᐅᑎᓂᖕᒋᓂᒃ ᓄᓇᐅᑦ ᖁᐊᖑᓂᖕᒐ ᐅᖁᓯᕙᓪᓕᐊᑎᓪᓗᒍ ᖃᓄᑎᒋ ᓄᓇᐅᑦ ᖃᖕᒐ ᐅᖁᓯᕙᓪᓕᐊᓕᕌᖕᒐᑦ ᖁᐊᖑᓂᖕᒐᓄᑦ ᑎᑭᐅᒪᑎᒋᖃᑦᑕᕐᓂᖕᒐ ᐊᒻᒪᓗ ᐊᓯᓪᓕᕐᐸᓪᓕᐊᓂᖕᒐ ᓄᓇᐅᑦ ᖁᐊᖑᓂᖕᒐᓄᑦ. ᑕᕙᓂ ᖃᐅᔨᓴᕐᓂᕐᒥ ᓇᓗᓇᐱᕐᓯᔪᒪᔪᒍᑦ ᑭᒃᓕᒋᔭᖕᒋᓐᓂᒃ ᐊᓯᕉᕈᓂ ᐅᑎᒃᑲᓐᓂᕈᓐᓇᐃᓕᕚᖕᒐᓂᒃ, ᐊᒻᒪᓗ ᐅᑎᕆᐅᒥᑦᑕᕐᓂᖕᒐᓂᒃ. (ᑐᕌᒐᐅᓪᓗᐊᑕᕐᑐᖅ ᑮᓇᐅᔭᕐᑖᕈᑎᒋᓗᒍ ᑕᕙᖕᒐᑦ NSERC ᑐᓂᔭᐅᔪᑦ). ᐊᕌᒍᖕᒐᓂ 2020 ᐊᐱᕐᑯᑎᖃᕐᑐᖕᒐ ᒪᕈᒃᓂᒃ ᖃᔪᓯᓯᒪᓪᓗᑎᒃ ᐊᕌᓂᒥᑦ 2019: (1) ᓄᓇᐅᑦ ᐊᐅᒪᓂᖕᒐ ᖄᖕᒐ ᓄᓇᐅᑦ ᖁᐊᖑᓂᖕᒐᓄᑦ ᖁᐊᖑᑎᑦᑎᕙ? ᐊᒻᒪᓗ (2) ᓂᓚᐃᑦ ᖃᑦᑎᒃᓯᓕᕐᓯᒪᔪᑦ ᓄᓇᒥ ᐊᔾᔨᒋᖏᑕᖕᒐᒍᑦ ᐊᐅᒃᐸᓪᓕᐊᓂᖃᕐᐸᑦ ᖁᐊᖑᓂᖕᒐᓂᑦ ᓄᓇᒦᑦ? ᖃᐅᔨᓴᕐᓂᓇᓂᐊᕐᑕᕗᑦ 2020 ᐱᖃᓯᐅᑎᓪᓗᓂ ᐆᒃᑐᕋᕐᑕᐅᓗᓂ ᐊᓯᓪᓕᕐᐸᓪᓕᐊᓂᖕᒐ ᓄᓇᐅᑦ ᖄᖕᒐ ᐊᑐᕐᓗᒋᑦ ᖃᐅᔨᓴᕈᑎᑦ ᑕᒻᒪᕇᒃᑯᑎᖃᕐᑐᑦ ᕿᓂᕈᑎᑦ ᒪᓂᕋᕐᒍᑦ ᓄᓇᐅᑦ ᐃᓗᐊᓄᑦ ᑕᑯᔪᓐᓇᕐᑐᑦ. ᑖᒃᑯᐊ ᖃᐅᔨᓴᕈᑕᐅᔪᑦ ᐱᖃᓯᐅᑎᓯᒪᓂᐊᕐᑐᑦ ᓄᓇᖑᐊᓕᕇᓂᕐᒎᑦ ᑎᑎᕋᕐᓯᒪᔪᓂ ᐊᑐᕐᑕᐅᓗᑎᒃᓗ ᖃᖕᒐᑦᑕᕐᑎᑕᐅᓯᒪᔫᒃᑯᑦ ᐊᔾᔩᓕᐅᕐᓯᒪᔪᓄᑦ, (b) ᖃᐅᔨᓴᕐᓂᖅ ᓄᓇᐅᑦ ᖄᖕᒐᓂᒃ ᐊᐅᒪᓂᖕᒐᓂᒃ ᐊᒻᒪᓗ ᐆᒃᑐᕋᕐᑕᐅᓗᑎᒃ ᐅᖁᓂᖕᒋᑦ ᒪᓴᐅᓂᖕᒋᓪᓗ ᐊᓯᓪᓕᕐᐸᓪᓕᐊᓂᖕᒋᑦ ᐊᐅᔭᐅᑦ ᕿᑎᐊᓂ. ᑲᑎᑦᑎᓂᐊᕐᑐᑦ ᐃᔾᔪᕐᓂᒃ ᐊᒻᒪᓗ ᓂᓚᒃᓂᒃ ᖄᖕᒐᓂᑦ ᐊᒻᒪᓗ ᐃᓱᐊᒥᓂᑦ ᖁᐊᖑᓂᖕᒐᑕ, ᐊᒻᒪᓗ (c) ᖃᖕᒐᑦᑕᕐᑎᑕᐅᓯᒪᔫᒃᑯᑦ ᖃᐅᔨᓴᕐᓂᖅ ᐊᓯᓪᓕᕐᐸᓕᐊᓂᐅᔪᓂᒃ ᓄᓇᖕᒐᓂ Fosheim Peninsula. ᑲᔪᓯᓚᐅᕐᓯᒪᖕᒋᑦᑐᖅ ᐊᕌᒍᖏᓐᓂ 2018 ᐊᒻᒪᓗ 2019 ᐊᑐᕐᑕᐅᓂᖕᒐ ᖃᐅᔨᓴᕈᑎ ᑕᑯᔾᔪᑎ ᓄᓴᒍᐊᒧᑦ ᓄᓇᒥ ᐊᓯᓪᓕᕐᐸᓪᓕᐊᓂᖕᒐᓂᒃ ᐊᐅᒃᐸᓪᓕᐊᓂᖕᒐᓂᒃᓗ. ᖃᕋᓴᐅᔭᒃᑯᑦ ᐊᐅᓚᔾᔪᑎᖕᒐ ᐋᕿᒃᓯᒪᓕᕐᑐᖅ ᑕᑯᔾᔪᑎ ᐋᕿᒃᓯᒪᓂᓕᕐᓂᐊᕋᓱᒋᔭᕗᑦ ᐊᑐᕐᓗᑎᒍ.

ᐊᑏᑎᖃᕐᓂᖕᒐ:

ᑖᓐᓇ ᖃᐅᔨᓴᕐᓂᖅ ᐃᑲᔫᑕᐅᓂᐊᕐᑐᖅ ᑐᑭᓯᔭᐅᓇᓱᒃᓗᓂ ᓄᓇᐅᑉ ᖁᐊᖑᓂᖕᒐ ᐊᒻᒪᓗ ᒪᓂᕋᕐᒥ ᓂᓚᐅᓂᖕᒐ ᖁᑦᑎᒃᑐᒥ ᐅᑭᐅᕐᑕᕐᑐᒥ. ᑐᑭᓯᔾᔪᑕᐅᓯᒪᓕᕇᕐᑐᖅ ᖃᐅᔨᔭᐅᓯᒪᖕᒋᑦᑐᓂᒃ ᓇᑭᖕᒌᕐᓯᒪᓂᖕᒐᓂᒃ ᐊᒻᒪᓗ ᐱᑐᖃᐅᑎᒋᓂᖕᒐᓂᒃ ᖁᐊᖑᓂᖕᒐ, ᖃᓄᑎᒋ ᐊᓯᓪᓕᕐᐸᓪᓕᐊᑎᒋᓂᖕᒐ ᐊᒻᒪᓗ ᐊᐅᒃᐸᓪᓕᐊᑐᐃᓐᓇᕆᐊᖃᕐᓂᖕᒐ ᓂᓚᐅᑦ ᓄᓇᒥ ᐊᒻᒪᓗ ᓂᓚᐃᑦ ᖃᑦᑎᒃᓯᓕᕐᓯᒪᔪᑦ ᓄᓇᒥ. ᖃᓄᑎᒋ ᐅᖁᓯᕙᓪᓕᐊᑎᒋᓂᖕᒐ ᐃᓯᒪᒋᔭᐅᓂᖕᒐ ᖁᑦᑎᒃᑐᒥ ᐅᑭᐅᕐᑕᕐᑐᒥ ᐃᒃᐱᖕᓇᐅᑎᖃᕐᓂᐊᕐᒪᑦ ᐊᕙᑎᖕᒐᓄᑦ ᓄᓇᖕᒐᓄᓪᓗ ᐅᑭᐅᕐᑕᕐᑐᒥ. ᑖᓐᓇ ᖃᐅᔨᓴᕐᓂᖅ ᐱᓪᓚᕆᐅᓂᖃᕐᑐᖅ ᐅᔭᖃᒃᓯᐅᐸᓪᓕᐊᑎᓪᓗᒋᑦ. ᑕᕗᖕᒐᕐᓯᔪᖕᒐ ᐅᓂᒃᖄᓕᐊᖑᓚᐅᕐᑐᒥᒃ ᖃᓄᐃᐸᓪᓕᐊᓂᖕᒐᓂᒃ ᓂᓚᒃ ᓄᓇᖕᒐᓂ Fosheim Peninsula.

ᕗᐊᐃᓐ ᐳᓪᓚᕐᑦ, ᐃᓕᓴᐃᔨᒻᒪᖅ
ᒪᒋᐅᓪ ᐃᓕᓐᓂᐊᕐᕕᒃᔪᐊᖅ

Appendix I :Recent Results
Under Nunavut Research Licence to Wayne Pollard

Project Title: An investigation of the sensitivity of high Arctic permafrost to climate change
Progress Report – 2019 Scientific Research Licence #02 027 19R-M (multiyear)

From MSc Project by Mr. Cameron Roy:

A Holocene glacial meltwater origin for massive ground ice in raised marine sediments in the Canadian High Arctic

1. Introduction

Ground ice is a dynamic feature of periglacial environments on Earth and Mars. From a geomorphic perspective, terrestrial landscapes underlain by massive ground ice (H_2O) are inherently unstable since it is a mineral with a melting point within the range of planetary temperatures. Assessments of the origins and age of massive ground ice bodies can be difficult and have long been one of the most contentious problems in permafrost geomorphology and planetary geocryology (e.g. MacKay 1971; French and Harry 1990; Vaikmae et al. 1993; Fritz et al. 2011). The main question is whether the massive ice is *i)* buried surface ice or *ii)* formed by *in-situ* freezing of subsurface water i.e. intrasedimental ice. Both types contain important information for paleoenvironmental reconstruction and landscape formation.

Many massive ground ice exposures in the Canadian High Arctic are found in proximity to present-day glacier ice or glacial depositional landforms and are thus interpreted as buried glacial ice, sometimes of Pleistocene-age (e.g. Dyke and Savelle 2000; Lakeman and England 2012; Coulombe et al. 2019). A notable exception are massive ice deposits found in the Eureka Sound Lowlands (ESL), which cover approximately 750 km^2 on Axel Heiberg and Ellesmere Islands. In the ESL, massive ground ice is found extensively in association with raised marine sediments and has been assigned an intrasedimental origin as a result of detailed analyses of the cryo-stratigraphy, spatial distribution and elevation of ground ice exposures (Pollard 1991, Pollard 2000a; Pollard et al. 2015). The current polar desert climate of the area is unable to supply the water to form such extensive ice deposits. The proposed source of the water and the relationship between the massive ground ice and the Last Glacial Maximum (LGM) remain poorly constrained. The objective of this research is to elucidate the water source, genesis and age of massive ground ice in the ESL based on the cryostratigraphic interpretation of environmental isotopes. More generally, we aim to *i)* provide insights into the process of massive ice formation in raised marine sediments and *ii)* demonstrate how a study of massive ice along an elevation transect can be used to reveal palaeoenvironmental information.

2. Study Area

In the Canadian High Arctic Archipelago, Eureka Sound (~290 km long, 13-48 km wide) separates Axel Heiberg Island from Ellesmere Island. The region is underlain by poorly lithified Tertiary sandstones, siltstones and shales of the Sverdrup Basin geologic structure (Bell and Hodgson 2000). The ESL includes the rolling coastal lowlands on both sides of Eureka Sound that are below 140-150 m a.s.l., which corresponds to the Holocene marine limit. The surficial material of the ESL is fine-grained sediment (silty clay to fine sand) interspersed with localized Holocene fluvial and coastal deposits and patches of thin organic muck (Hodgson 1985). Massive ground ice is found exclusively within these fine-grained marine sediments (Hodgson and Nixon 1998; Pollard 2000a,b), hence the focus on land below marine limit. The Fosheim Peninsula, on Ellesmere Island, comprises most of the 750 km^2 area of the ESL.

The long-term mean annual air temperature observed at Eureka Weather Station is -19.7°C and the mean annual precipitation is < 70 mm, making it one of the driest places in Canada (Environment

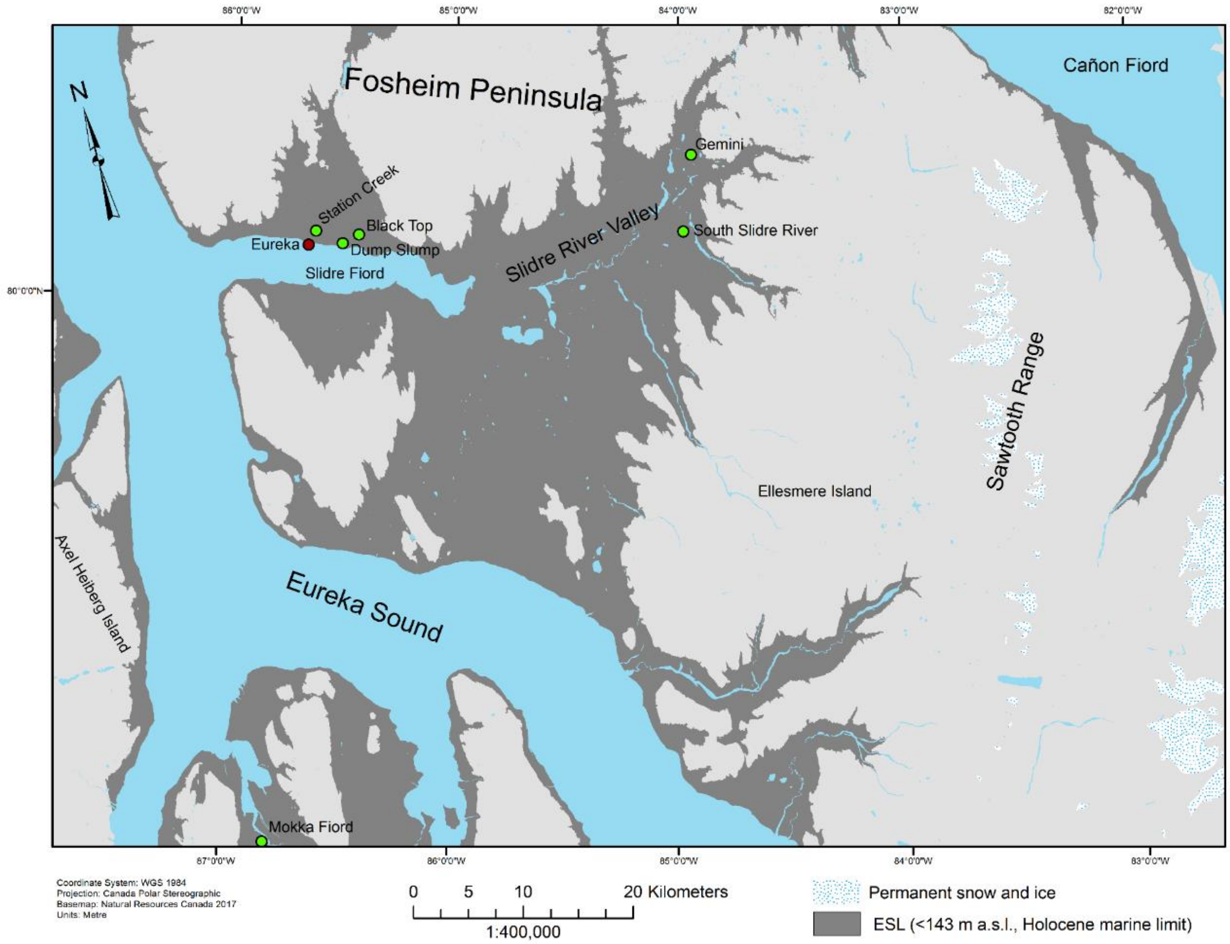

Figure 1: Map of massive ground ice study sites in the Eureka Sound Lowlands (ESL).

Canada). The ESL are characterized by deep, continuous permafrost. According to Taylor (1991) the permafrost depth is 500 m. The active layer depth is typically ~60 cm but varies due to microclimatic conditions. Mean annual ground temperatures are stable around -16.5°C, and the depth of zero annual amplitude is 15.4 m (Pollard et al. 2015).

According to England et al. (2006), at the time of the LGM Eureka Sound was an ice saddle where ice flowing west of the Ellesmere Ice Divide coalesced with ice flowing east from the Axel Heiberg alpine divide. Glacial isostatic adjustment models predict the Eureka Sound intermontane region would have been inundated by up to 1200 m of trunk ice; the maximum loading of the entire Innuitian Ice Sheet (Ó Cofaigh et al. 2000; Simon et al. 2015). Disintegration of the central part of the ice sheet began in earnest ~9.0 ka and the sea penetrated the Eureka Sound intermontane area between 8.5 and 8.0 ka, inundating the length of Eureka Sound (England et al. 2006).

Based on the cryo-stratigraphy of the exposures, Pollard (2000b) interpreted the ESL massive ice as having a segregated-intrusive origin, synchronous to Holocene permafrost aggradation and marine regression. Previous research focused on mapping and stratigraphic relationships, quantifying ground ice volume (Couture and Pollard 1998; Bernard-Grand'Maison and Pollard 2018), retrogressive thaw slump behaviour (Ward-Jones et al. 2019), active layer detachments (Lewkowicz 2007) and ground ice microbiology (Steven et al. 2007). This study is the first to present high-resolution geochemical profiles of ESL massive ground ice.

3. *Methods*

While massive tabular ice underlies much of the ESL (Hodgson and Nixon 1998; Pollard 2000a), it is most easily sampled from natural exposures in retrogressive thaw slumps. For this study, we sampled ice from slumps along an elevation gradient, from Holocene marine limit (~143 m a.s.l.) to modern sea level (Slidre Fiord). The stratigraphic position of each massive ice exposure was described and recorded.

3.1) Field sampling

At each exposure we collected cores at multiple locations adjacent to the slump headwall in 2017. Two strategies were used to extract cores containing massive ground ice:

1. Where there was < 2 m of sediment overlying massive ice, a pit was dug to the top of the permafrost table. Active layer (AL) soil was sampled with a trowel at 5 cm intervals. AL samples were stored in sealed polyethylene bags. A Snow, Ice and Permafrost Research Establishment (SIPRE) corer attached to a handheld motorized power head was used to extract 3” diameter vertical cores from the permafrost. The cores ranged from 40-160 cm in length, with the goal to sample the upper contact and as much of the massive ice body as possible. The frozen cores were preserved in 5-75 cm segments, wrapped in aluminum foil, labelled and stored in thermally-insulated boxes.
2. If overlying sediments were > 2 m, cores were drilled directly into the ablating massive ice surface by constructing a safe drilling platform above the mudflow. Frozen samples were preserved in the same manner as described above.

Frozen cores were transported to the CryoLab at the University of Ottawa. Permafrost cores were supplemented with individual grab samples from the (cleaned) ablating ice face and overlying frozen sediments.

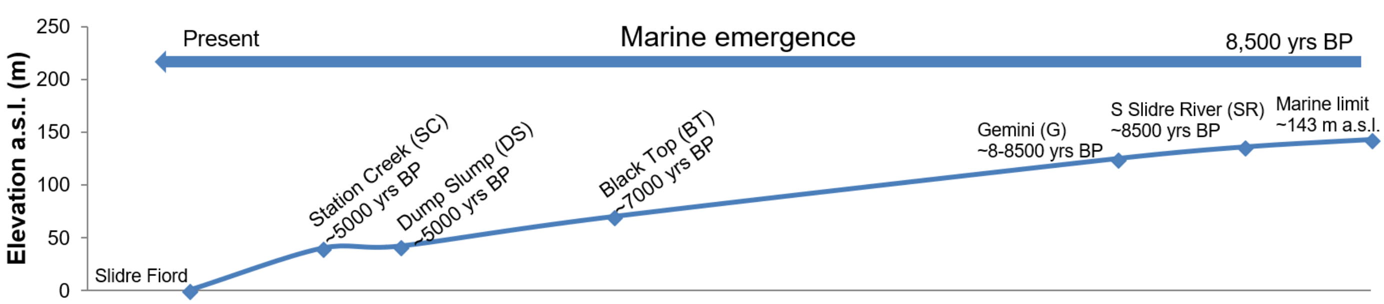

Figure 2: Schematic diagram of elevation transect of massive ice exposures on the Ellesmere Island side of the ESL. Marine emergence dates are based on Simon et al. (2015)’s revised Innuitian Ice Sheet model for relative sea level (RSL) in the Eureka area during the Holocene. The geophysical model is constrained by field RSL data derived from the ages and elevations of radiocarbon-dated material, such as marine shells, driftwood and mammal bones.

In addition to the elevation transect of exposed ground ice, water was sampled (stored in 20 ml HDPE vials) from several natural sources in the ESL: Slidre Fiord (79°58'17.8"N, 85°41'50.7"W), Mokka Fiord (79°35'6.9"N, 86°46'33.2"W), two late-lying snowbanks (79°59'58.3"N, 85°47'47.4"W; 79°59'52.8"N, 85°46'20.0"W) and Black Top Creek (79°58'50.4"N, 85°4'36.4"W).

Additionally, samples were collected from ice wedges that were exposed in cross-section in the headwalls of slumps. "Edge" and "Centre" samples were taken, representing older and younger ice, respectively. The ice was melted in sealed polyethylene bags in the field, and then transferred into dark HDPE bottles.

3.2) Active layer samples

The 5 cm interval AL soil samples were analyzed for gravimetric moisture content (% dry weight), colour (dry), loss-on-ignition (%), texture (sand, silt, clay %), $\delta^{13}C$ (‰), bulk organic C (%), $\delta^{15}N$ (‰) and total N (%). AL samples were weighed, dried at 105°C for 24 hours and then re-weighed. Gravimetric moisture content (GMC) was calculated as:

GMC *(%) = (Pre-dry mass – Post-dry mass)/Post-dry mass * 100*

The colour of the dried soil was recorded using the Munsell colour system. It was then ground with a mortar and pestle to prepare for loss-on-ignition (LOI) analysis with a thermogravimetric analyser (Leco TGA701). To prepare for texture analysis, 5 ml of AL soil was dispersed with 40 ml of sodium hexametaphosphate. A laser diffraction analyser (Microtrac S3500) was used to assess the proportions of sand, silt and clay-sized particles. Bulk C and N analyses were performed by Y. Wang at the University of Ottawa on acidified sediment samples with an *Elementar VarioEL III* instrument.

3.3) Permafrost samples

Since the objective was to create high-resolution depth profiles of the massive ice for isotope analysis; the permafrost cores were first sliced longitudinally; one half was archived in a -17°C freezer while the remaining half was cut into 2 cm-thick sub-samples ("half-pucks") with a modified circular saw in the CryoLab which were melted in sealed 50 ml sterile centrifuge tubes. Sub-samples were analyzed for excess ice (% of total volume that is greater than saturation), volumetric ice content (% total volume) and gravimetric ice content (% dry weight). Sediment was analyzed for texture (sand, silt, clay %), loss-on-ignition (%), $\delta^{13}C$ (‰), bulk organic C (%), $\delta^{15}N$ (‰) and total N (%). Supernatant water was analysed for stable water isotopes (δD, $\delta^{18}O$, *d* excess), major cations (Ca^{2+}, Fe^{2+}, K^+, Mg^{2+}, Na^+, Sr^{2+}), anions (SO_4^{2-}, Cl^-, NO_3^-), dissolved organic carbon (DOC) and dissolved organic nitrogen (DON).

First, the thawed samples were weighed and then centrifuged for 5 minutes at 5000 rpm to help separate the mixture (soil and water). The volume of supernatant water was recorded. The supernatant water (filtered through 0.45µm pore diameter) was put into 20 ml vials for stable water isotope and ion analyses. The sediment was dried at 105°C for 24 hours and re-weighed. This was used to calculate the gravimetric ice content (GMC, or *W*) with the same formula as outlined in *Section 3.2*. The volumetric ice content (fV_i) was calculated according to the procedure given by Pollard and French (1980): $fV_i = V_i/(V_i + Vs)$, where: $V_i \approx W + (0.09W)$, V_i = volume of ice and Vs = volume of soil solids.

A Los Gatos Research (LGR) liquid water analyser coupled to a CTC LC-PAL autosampler was used for simultaneous $^{18}O/^{16}O$ and D/H ratios for H_2O. ^{18}O and D are measured relative to VSMOW (‰). Deuterium excess (*d*) excess was calculated following Dansgaard 1964. Samples were analyzed for stable water isotopes whenever at least 2 ml of supernatant water could be extracted from the sub-samples.

Major cations (Ca^{2+}, Fe^{2+}, K^+, Mg^{2+}, Na^+, Sr^{2+}) and anions (SO_4^{2-}, Cl^-, NO_3^-) were measured on supernatant water from *every second* sub-sample for at the geochemistry laboratory at the Advanced Research Centre at the University of Ottawa. Prior to cation analysis, water samples were acidified to a pH of 2 with ultra-pure HNO_3 acid. Anion samples were not acidified. Cation and anion samples were diluted with deionized water by a factor of 10. An inductively coupled plasma atomic emission spectrometer (ICP-AES) measured concentrations of the ions, with duplicate samples run (analytical reproducibility < 5%). Ionic concentrations for the ground ice are presented in mg/l.

A Shimadzu TOC analyser (*Vcsn* model) was used to measure DOC/TN. First, meltwater sub-samples were acidified to a pH of 3 - to help remove dissolved inorganic carbon (DIC) by sparging with Ultra-Zero compressed air for 5 minutes prior to analysis. The DOC measured in this analysis is specifically Non-Purgeable Organic Carbon (NPOC), as opposed to DOC calculated as Total Carbon (TC) – Inorganic Carbon (IC). The analyser uses a platinum catalyst for high-temperature combustion (720°C) of acidified samples, then passes them through a non-dispersive infrared detector. It takes the best 3 of 5 sample injections and provides the mean, with a coefficient of variation <5%. TN is measured off peaks produced by the detection of nitrogen monoxide gas – which itself is the product of the decomposition of TN in the sample upon combustion. DOC/TN was only analyzed on select massive ice samples, ice wedges and environmental samples (e.g. snowbank).

All sediment samples from the cores were measured for LOI and select sediment samples for texture (sand, silt, clay %) using the same methods outlined in *Section 3.2*.

4. *Results*

4.1.1) Dump Slump (2 cores: DS-1, DS-2) – 40 m a.s.l.*

The mean bulk C content of DS-1 sediment is 2.15%. Sediment within massive ice has significantly higher bulk C content (2.49%) compared to AL soil (1.66%) ($p=0.004$). The mean $\delta^{13}C$ of DS-1 sediment is -25.03‰. There is no significant difference between the $\delta^{13}C$ signature of AL sediment and sediment within massive ice. The mean bulk N content and $\delta^{15}N$ of DS-1 sediment are 0.13% and there is no significant difference between AL and permafrost sediment for either variable. The mean C:N ratio is 16:1, with a significantly lower mean C:N ratio in AL soil (~14:1) compared to sediment within massive ice (~17:1) ($p=0.04$).

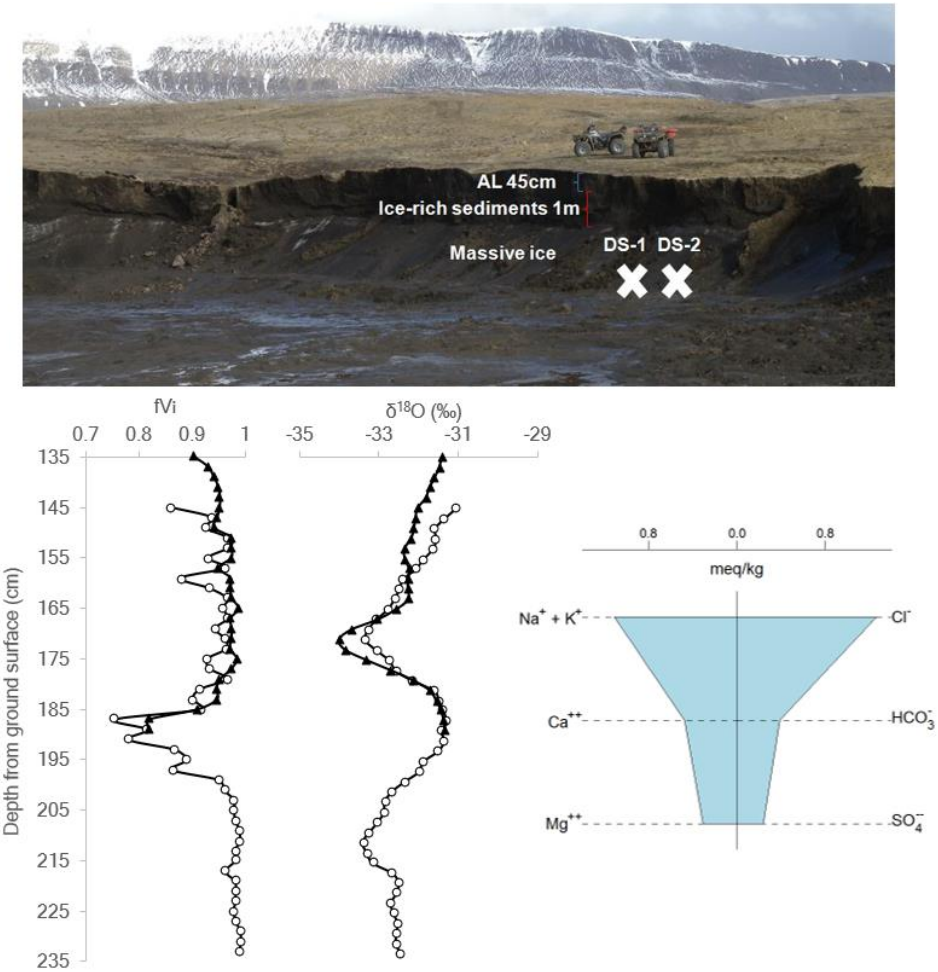

Figure 3: Dump Slump (40 m a.s.l.). Volumetric ice content (fVi) and $\delta^{18}O$ of DS-1 (circle) and DS-2 (triangle) cores, geochemical facies of DS-1 ice.

The volumetric ice content (fV_i) of core DS-1 is high, with a mean of 94.0%, ranging from 75.4 to 99.1%. Core DS-2 is also ice-rich, with a mean of 94.7%, ranging from 81.8 to 98.7%.

Stable water isotopes are depleted in both DS-1 and DS-2 cores. In DS-1, δD ranges from -258.0 to -237.9‰ and $\delta^{18}O$ from -33.3 to -31.1‰. In DS-2, δD ranges from -265.6 to -245.7‰ and $\delta^{18}O$ from -34.0 to -31.3‰. The δD-$\delta^{18}O$ slopes of DS-1 and DS-2 are 7.78 and 7.26, respectively. There is no significant relationship between dD and *d* in DS-1 and a weak negative relationship in DS-2. Total dissolved solids (TDS) in DS-1 ice range from 33 to 8833 mg/l, with a median of 160 mg/l. The dominant ions are $(Na^{+}+K^{+})/Cl^{-}$. DOC concentrations in massive ice ranged from 2.36 to 2.41 mg/l.

4.1.2) Station Creek (2 cores: SC-1, SC-2) - 45 m a.s.l.*

The fV_i of core SC-1 is very high, with a mean of 93.1%, a minimum of 56.7% and a maximum of 100%.

Stable water isotopes are highly variable in SC-1 ice, with δD ranging from -268.6 to -196.0‰ and $\delta^{18}O$ from -34.9 to -25.5‰. The δD-$\delta^{18}O$ slope is 7.52 and there is no significant relationship between δD and *d*. TDS values vary from 28 to 1152 mg/l, with a median of 154 mg/l. The dominant ions are $(Na^{+}+K^{+})/Cl^{-}$. DOC concentrations in SC-1 ice range from 1.73 to 19.47 mg/l.

Ice from reticulated veins in a clay layer just above SC-1 ice has δD ranging from -119.9 to -117.2‰ and $\delta^{18}O$ ranging from -16.7 to -15.8‰. DOC concentrations in the reticulated ice is measured at 1.79 mg/l.

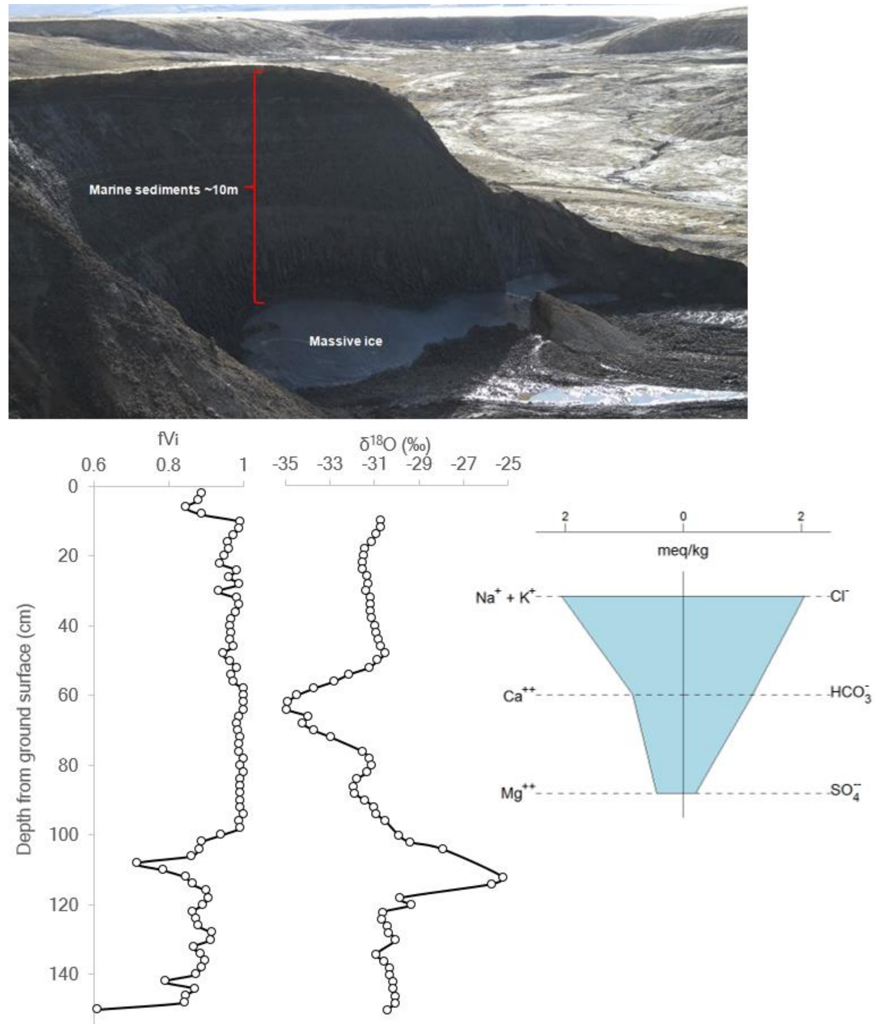

Figure 4: Station Creek (45 m a.s.l.) Volumetric ice content (fVi) and $\delta^{18}O$ of SC-1 core (circle), geochemical facies of SC-1 ice.

4.1.3) Black Top (2 cores: BT-1, BT-2) – 70 m a.s.l.*

The mean bulk C content of BT-2 sediment is 2.72%. Permafrost sediment has a significantly higher bulk C content (2.88%) compared to AL soil (2.27%) ($p<0.001$). The mean $\delta^{13}C$ of BT-2 sediment is -25.12‰. There is no significant difference between the $\delta^{13}C$ signature of AL sediment and permafrost sediment. The mean bulk N content and $\delta^{15}N$ of BT-2 sediment are 0.14% and 2.77‰, respectively. The $\delta^{15}N$ of AL soil is significantly enriched (3.14‰) compared to permafrost soil (2.64‰) ($p<0.001$). The mean C:N ratio is 19:1, with a significantly lower mean C:N ratio in AL soil (16.5:1) compared to sediment within massive ice (~20:1) ($p<0.001$).

The fV_i of cores BT-1 and BT-2 are moderately high with means of 71% and 57%, respectively. BT-1 fV_i values range between 39.0 and 89.7%, while BT-2 ranges between 14.8 and 85.8%.

Stable water isotopes are more enriched in BT-1 and BT-2 than cores from other sites. In BT-1, δD ranges from -213.2 to -171.6‰ and $\delta^{18}O$ from -27.8 to -20.8‰. In BT-2, δD ranges from -187.2 to -175.8‰ and $\delta^{18}O$ from -24.5 to -22.7‰. The δD-$\delta^{18}O$ slopes of BT-1 and BT-2 are 6.52 and 5.75, respectively. There are significant negative relationships between δD and *d* in both cores. BT-2 ice has very high TDS concentrations, ranging from 6,913 to 34,152 mg/l, with a median of 14,094 mg/l. The dominant cation is Na^+. The dominant measured anion is Cl^-, although charge balance analysis suggests that HCO_3^- (unmeasured) may be present in high concentrations as well.

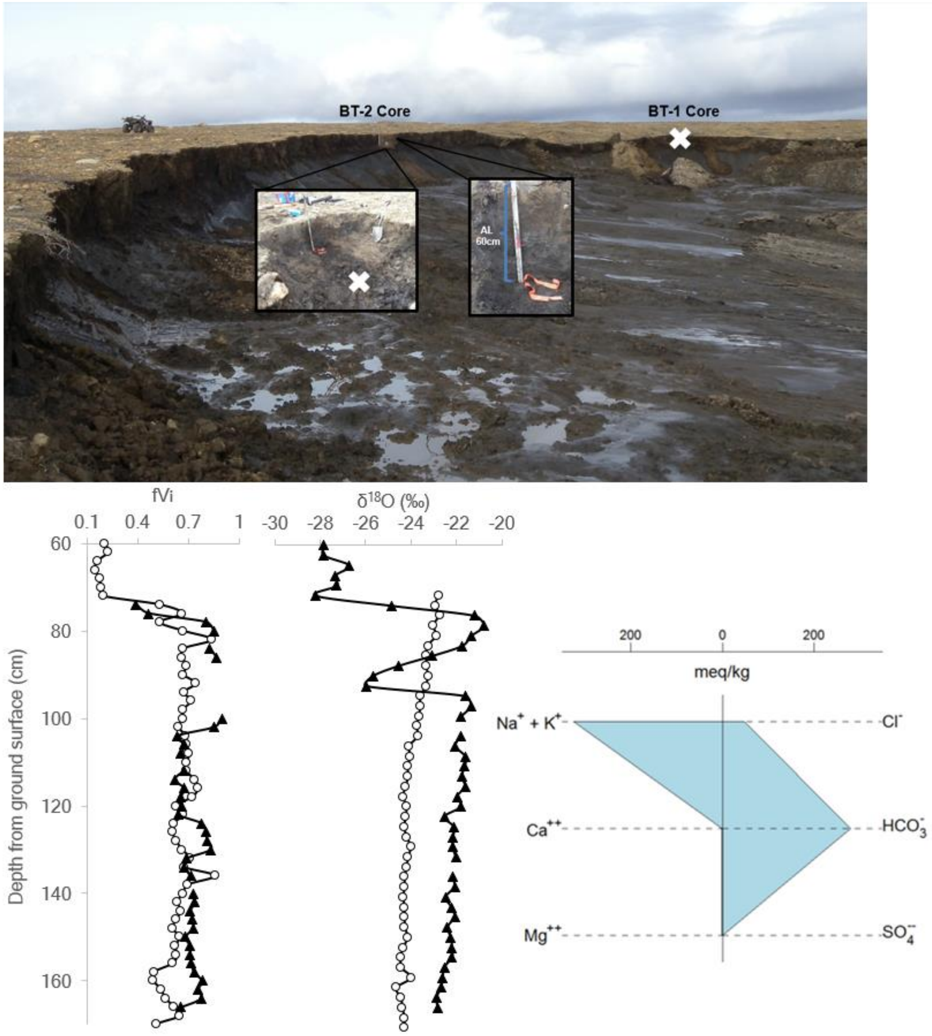

Figure 5: Black Top (70 m a.s.l.). Volumetric ice content (fVi) and $\delta^{18}O$ of BT-1 (circle) and BT-2 (triangle) cores, geochemical facies of BT-2 ice.

4.1.4) Gemini (2 cores : G-1, G-3) – 120 m a.s.l.*

Mean bulk C content of sediment in the G-3 core is 2.99%. Mean $\delta^{13}C$ is -25.5‰. There is no significant difference in C content or isotopic signature between sediment from above or within the massive ice. Mean bulk N content is 0.22% and the mean $\delta^{15}N$ is 2.54‰. The mean C:N ratio is 14:1. N analyses were only done on sediment within the massive ice.

Massive ice in the G-1 and G-3 cores have very high fV_i, with means of 98% and 96%, respectively (excluding samples of sediment above massive ice). There is very little variation in fV_i within the massive ice of G-1 and G-3. G-1 ranges between 97.0 and 98.9%, while G-3 ranges between 87.4 and 97.6%.

Stable water isotopes are consistently depleted. In G-1, δD ranges from -263.3 to -249.1‰ and $\delta^{18}O$ from -33.9 to -32.1‰. In G-3, δD ranges from -243.0 to -223.5‰ and $\delta^{18}O$ from -31.5 to -29.8‰.

The δD-δ^{18}O slopes of G-1 and G-3 are 7.33 and 8.43, respectively. There is no significant relationship between δD and *d* in either G-1 or G-3. The TDS concentration in G-3 ice is low, between 25 and 606 mg/l, with a median of 36 mg/l. The dominant cation is Ca^{2+} and a charge balance analysis implies that HCO_3^- is the dominant anion. DOC concentrations in G-3 ice range from 3.26 to 4.40 mg/l.

4.2) Comparison with local water sources

Modern water sources in the ESL include Slidre Fiord, Black Top (BT) Creek and the snowpack (Table 1). Massive ground ice samples are isotopically depleted compared to these modern water sources, except for Black Top massive ice, which was in the range of BT Creek and snow. Figure 7 demonstrates the variation in TDS among massive ice exposures compared with brackish Slidre Fiord and the snowbank. TDS concentrations vary over four orders of magnitude within ESL massive ice.

Black Top massive ice has TDS concentrations that exceed fiord water.

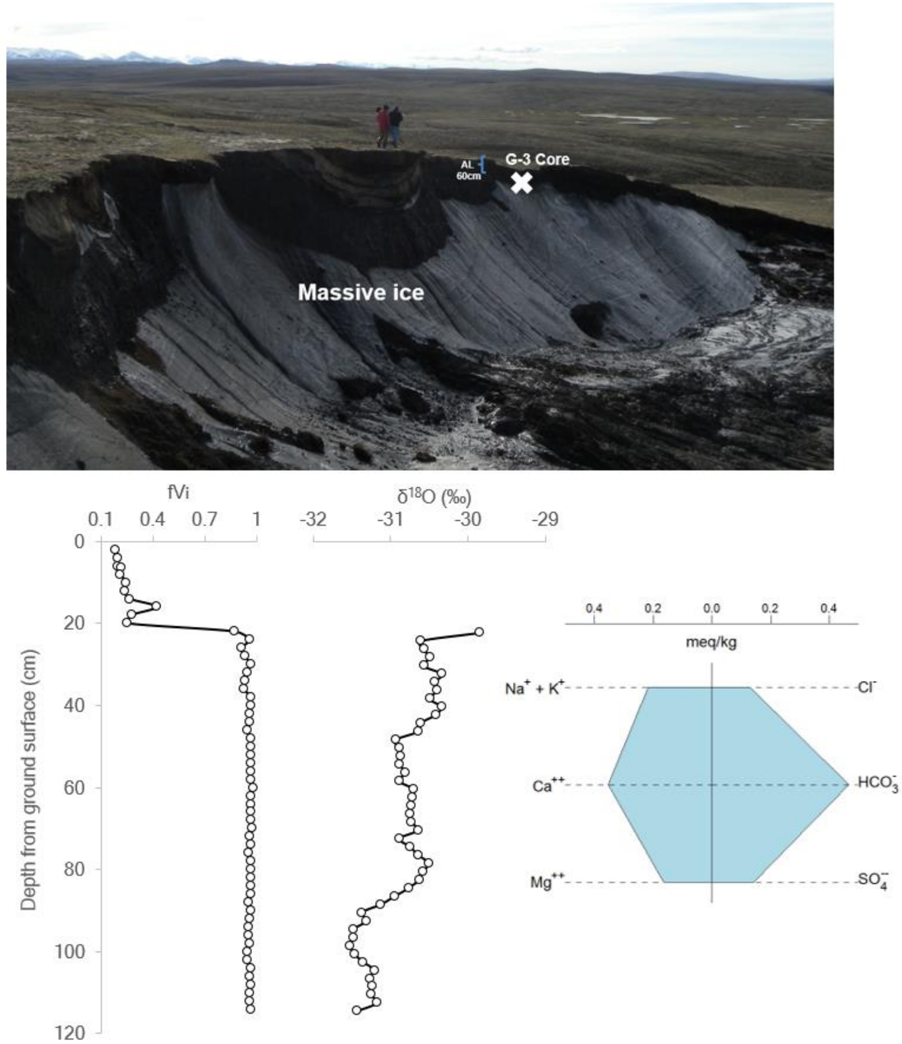

Figure 6: Gemini (120 m a.s.l.). Volumetric ice content (fVi) and δ^{18}O of G-3 core (circle), geochemical facies of G-3 ice.

Source	δD	δ^{18}O	*d*	Ca^{2+}	Fe^{2+}	K^+	Mg^{2+}	Na^+	Sr^{2+}	SO_4^{2-}	NO_3^-	Cl^-
		‰						*mg/l*				
Slidre Fiord	-98.35	-13.21	7.34	117.0	<0.01	79.61	199.3	1621.1	1.33	595.8	*nd*	4414.6
BT Creek	-189.36	-24.83	9.24	24.47	<0.01	1.48	10.21	10.84	0.08	73.00	0.08	13.51
Late-lying snowbank	-220.23	-28.77	9.93	0.99	0.08	0.69	0.28	3.12	<0.01	0.55	0.12	1.70

Table 1: Stable water isotopes and major ions in local water sources: Slidre Fiord (sampled at 79°58'17.8"N, 85°41'50.7"W), Black Top (BT) Creek (sampled at 79°58'50.4"N, 85°4'36.4"W) and a late-lying snowbank near the Eureka airstrip (79°59'58.3"N, 85°47'47.4"W).

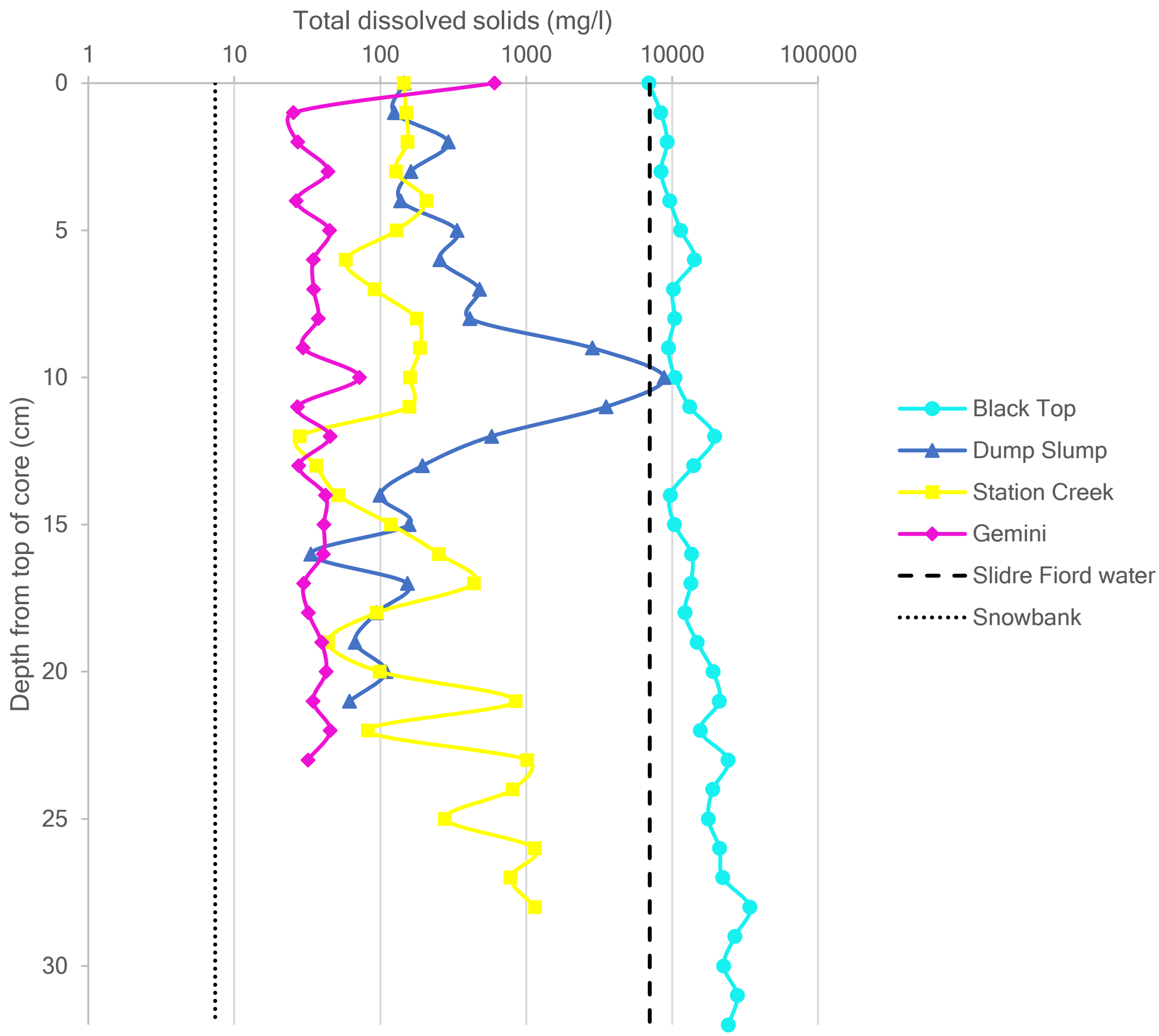

Figure 7: Total dissolved solids (TDS) in melted ground ice in permafrost cores from the ESL. TDS in Slidre Fiord water and a late-lying snowbank are given as reference.

5. *Discussion*

5.1) Origin of massive ice:

The primary aim of this research is to confirm the origin of the massive ice deposits in the ESL. In the landscape model presented by Pollard (2000b), which forms the framework of this study, groundwater is driven by a hydraulic and thermal gradient from an aquifer (mainly poorly consolidated bedrock) underlying Holocene marine sediments to a freezing front induced by marine emergence.

Co-isotope plots (δD-δ^{18}O) are often used to help determine the origin of ground ice, based on the theory that buried glacier ice will have a freezing slope close to the meteoric line (~ 8), while segregated ice (i.e. formed by slow equilibrium-freezing) will have a slope <6. The LMWL measured at Eureka Weather Station follows a slope of 7.4 (IAEA 2018). At every ESL site except Black Top, the massive ice has a co-isotope slope ≥ 7.4 (Table 2). This would suggest that much of the massive ice in the ESL is derived from buried glacial or snowbank ice, contrary to the hypothesis of Pollard (2000a&b) and Pollard et al. (2015).

Sample	Co-isotope slope
Global meteoric water line **(GMWL)**	**8**
Local meteoric water line at Eureka **(LMWL)**	**7.4**
DS-1	7.78
DS-2	7.26
SC-1	7.52
BT-1	6.52
BT-2	5.75
G-1	7.33
G-3	8.43

Table 2: Co-isotope slopes of ESL ground ice and local precipitation.

However, a buried ice origin is rejected for most ESL massive ice. A segregated-intrusive origin of ESL massive ice is more likely for several reasons:

1) In almost all cases, ESL massive ice is found stratigraphically below laminated fine-grained marine sediments. The upper contact between the ice and the overlying marine sediments is conformable and gradational, as would be expected where intrasedimental ice forms epigenetically in the marine sediments following emergence. Marine sediments also occur as thin layers within the upper part of the massive ice. The internal structure of the massive ice is consistently horizontal to sub-horizontal and concordant with the structure of the overlying sediments. The sites analysed are stratigraphically similar to the several hundred other sites documented as part of a long-term study on ground ice in the ESL (Pollard et al 2015).

2) Widespread preservation of substantial volumes of glacial ice in a submarine setting is highly unlikely, although theoretically possible. Recent studies by Overduin et al. (2012) and Stendel et al. (2016) have demonstrated the widespread existence and persistence of sub-sea permafrost, but large volumes of relict glacier ice have not been documented under the sea. In most cases submarine permafrost is associated with the post glacial inundation of coastal lowlands that already contained extensive permafrost (e.g. the Beaufort Shelf).

3) There is chemical continuity between the massive ice and ice lenses found in the overlying marine sediments, as well sediment inclusions in the massive ice match the texture of the overlying marine sediments. In some cases the overlying marine sediments are in excess of 5 m thick and finely laminated indicating prolonged submergence. The presence of bivalves in growth position (Bell and Hodgson 2000) also indicate a relative stable submarine environment.

4) Glacial till is conspicuously absent in massive ice exposures and for the most part anywhere in the ESL. Sediments mapped as till by Bell (1996) tend to be relatively patchy and thin.

Even though these points do not explain the “meteoric” freezing (co-isotope) slopes observed in ESL massive ice, it is widely understood that in an open system where there the input of isotopically-depleted water is much greater than the freezing rate, “meteoric” freezing slopes can be produced in segregated ice, as would be the case if local glacial meltwater was the primary source for ground ice formation (e.g. French and Harry 1990, Rampton 2001).

Souchez and Jouzel (1984) give the following equation for a freezing slope (s) in an open system with an initial reservoir (i) and input (A) at t=0:

$$s = \frac{\alpha[(\alpha - 1)(1 + \delta i) - (A/S)(\delta A - \delta i)]}{\beta[\beta - 1)(1 + \Delta i) - (A/S)(\Delta A - \Delta i)]}$$

where β = fractionation factor of ^{18}O ice-water, α = fractionation factor of D ice-water, δA = input D (‰), δi = reservoir D (‰), ΔA = input ^{18}O (‰), Δi = reservoir ^{18}O (‰), A = coefficient for input and S = coefficient for freezing.

This equation shows that the freezing slope depends on (δA-δi) and (ΔA-Δi), i.e. the difference between the δ value of the input and that of the reservoir at t=0. Souchez and Jouzel (1984) write that “in a natural reservoir, generally there is no reason for a change of input during the formation of this reservoir and during it subsequent freezing”. They argue that in natural settings δA=δi and ΔA=Δi, so the slope equation reduces to:

$$s = \frac{\alpha[(\alpha - 1)(1 + \delta i)]}{\beta[\beta - 1)(1 + \Delta i)]}$$

Thus, the freezing slope for an open system is essentially the same as it is for a closed system, as long as the input is not significantly different in its isotopic composition from that of the initial reservoir. This model predicts that under equilibrium freezing (as would be expected for the ice segregation), the freezing slope should plot significantly below the meteoric slope. Souchez and Jouzel (1984) is the theoretical foundation of most subsequent studies using co-isotope plots to determine ground ice origin.

Souchez and de Groote (1985) published evidence of a natural exception to the assumption of similar isotopic signatures in an open freezing system. At the Gruben-*gletscher* in Valais, western Switzerland, basal ice forms where subglacial meltwater enters a permafrost zone near the glacier margin and freezes at the glacier sole. There is also seepage of water from an ice-dammed lake into this zone near the glacier margin. They found the δD-$\delta^{18}O$ slope of the basal ice to be ~8.3, much higher than predicted by Souchez and Jouzel’s (1984) model for open-system freezing. To explain this, Souchez and de Groote (1985) ran a computer simulation for the evolution of δD and $\delta^{18}O$ in ice samples if the reservoir is allowed to mix over time with an isotopically-lighter input. They found that under the conditions observed at the base of Gruben-*gletscher* (where the input of isotopically-depleted water is much greater than the freezing rate), basal ice samples will plot along a “meteoric” slope – albeit with slightly lower *d* excess values. This effectively negates the use of the slope of co-isotope plots to distinguish between glacial ice and ice formed by equilibrium freezing, under the scenario observed at Gruben-*gletscher*.

Another natural example of “meteoric” slopes produced by an open freezing system with an isotopically-light input is found at the Mammuthöhle cave in the Alps of central Austria. Kern et al. (2011) found a freezing slope of 8.13 in a 5 m core from perennial cave ice deposits. They realized that most of the ice accumulation occurred in the early spring when karst spring water (which represents an average isotopic signature of yearly precipitation) receives an influx of snow meltwater (with a more depleted isotopic signal), as it slowly freezes on the cave floor.

The two conditions outlined by Souchez and de Groote (1985) required to produce “meteoric” slopes in ice formed by equilibrium freezing are: 1) an open system where a reservoir is well-mixed with an isotopically-lighter input and 2) a slow freezing rate. The landscape model for massive segregated ice formation in the ESL (Pollard et al. 2015) or, for that matter, any massive segregated ice associated with the deglaciation of an ice sheet and permafrost aggradation along its margins in the style of Rampton (1988, 1991), fit these criteria. In the case of the ESL:

1) The two isotopically-disparate water sources would be an initial reservoir of isotopically-heavy remnant seawater within the raised marine sediments and isotopically-depleted glacial meltwater being driven to the glacier terminus. Modern Slidre Fiord seawater is measured at $\delta D \approx -98‰$ and $\delta^{18}O \approx -13‰$, compared to glacial meltwater which has an isotopic signal closer to $\delta D \approx -250‰$ and $\delta^{18}O \approx -30‰$ (e.g. Lecavalier et al. 2017).

2) The theory behind the growth of massive segregated ice lenses, as explained in Section 1.3.2 (pp. 11-13), necessitates a slow freezing rate, i.e. a stable freezing front, to allow unfrozen groundwater to migrate upwards to the freezing front over long periods of time (10^2-10^3 yrs).

More evidence for a mixed water source is given by the hydrochemical facies observed in ESL massive ice. The facies of massive ice samples from Dump Slump and Station Creek (~40-50 m a.s.l., emergence ~5 kya) are Na-Cl dominant and almost identical to modern Slidre Fiord water, but with TDS concentrations lower by more than one order of magnitude (Figure 7). The highly-depleted stable water isotope values in the ice confirm that in spite of the clear marine influence, the primary water source for the ice has to be meltwater, not marine water.

The only massive ice that shows a "classic" freezing slope is at Black Top slump (~70 m a.s.l., emergence ~7,000 yrs BP), with slopes of 5.75 and 6.52 from cores BT-1 and BT-2, respectively. Black Top ice is also more sediment-rich (i.e. lowest volumetric and gravimetric ice content among ESL massive ice samples). According to the theory of ice segregation, the inclusion of more sediment into the Black Top ice is an indicationof a faster freezing rate, as there is no discernible difference in sediment particle size at Black Top compared to Dump Slump or Station Creek. A faster freezing rate would prevent the long-term migration of underlying groundwater – thus with the Pollard et al. (2015) model in mind, we would expect less of a ‘glacial’ signal and more of ‘marine’ signal. The reduced mixing also explains why the δD-$\delta^{18}O$ slope plots along a lower line – the site is more representative of a closed freezing system. The TDS concentrations measured in Black Top ice are in the range of modern Slidre Fiord water (>10,000 mg/l) (Figure 7) and its Na^+ concentrations exceed all other ESL massive ice by two orders of magnitude. The $\delta^{18}O$ values of Black Top ice range from -27 to -20‰ (Figure 5), significantly heavier than Dump Slump and Station Creek ice, but also lighter than modern fiord water (-

13‰). However, it is expected that during the Holocene the isotopic signal of Slidre Fiord would become heavier over time. At the time of when marine sedimentation was occurring at Black Top, Slidre Fiord would have been receiving substantial amounts of isotopically-depleted meltwater from the deteriorating Innuitian Ice Sheet that fringed it. There is a high probability that the $\delta^{18}O$ value of ~ -22‰ VSMOW found in Black Top ice is closer to early Holocene Slidre Fiord $\delta^{18}O$ than our modern measurement.

As further evidence of a marine influence, the calculated $(Na^{+}+K^{+})/Ca^{2+}$ and Cl^{-}/HCO_3^{-} ratios for ESL massive ice and other sources are presented in Table 3. In their study into the origin of massive ground ice on Herschel Island, N.W.T., Fritz et al. (2011) write that "$(Na^{+}+K^{+})/Ca^{2+}$ and Cl^{-}/HCO_3^{-} ratios greater than unity [>1] indicate an enrichment of ions with a likely marine origin derived from dissolution from sediments with a marine influence." Dump Slump and Station Creek massive ice samples have ratios > 1, while Black Top ice is >> 1. The only massive ice that deviates from this trend is at the Gemini site.

Massive ice at Gemini (~120-130 m a.s.l., emergence ~8.5 kya) is very pure (few to no sediment inclusions) and has a thinner sediment overburden (<2 m). Stable water isotope profiles in cores G-1 and G-3 reveal depleted δD and $\delta^{18}O$ values that remain constant with depth (Figure 6). $\delta^{18}O$ values are on average ~ 3‰ more depleted in G-1 core (lower) compared to G-3 core (higher). The stratigraphic vertical difference between G-1 and G-3 is about 10-15 m.

Site	$(Na^{+}+K^{+})/Ca^{2+}$ ratio					Cl^{-}/HCO_3^{-} ratio				
	N	Mean	Median	Min.	Max.	N	Mean	Median	Min.	Max.
Dump Slump massive ice	14	7.17	2.34	0.60	66.23	14	4.40	3.38	1.94	10.96
Black Top massive ice	32	343.33	350.20	166.18	507.75	32	51.18	54.22	24.72	71.26
Station Creek massive ice	28	4.23	2.41	1.07	22.12	28	3.94	2.36	1.11	18.25
Gemini massive ice	**23**	**0.66**	**0.58**	**0.29**	**1.31**	**24**	**0.44**	**0.36**	**0.13**	**1.15**
Pore ice in sediment above Gemini ice	1	68.28	/	/	/	1	2.73	/	/	/
Slidre Fiord water	1	12.43	/	/	/	1	21.32	/	/	/
Black Top Creek water	**1**	**0.33**	**/**	**/**	**/**	**1**	**0.57**	**/**	**/**	**/**
Glacial ice (west Greenland)*	**3**	**0.72**	**/**	**0.64**	**0.78**	**2**	**0.36**	**/**	**0.29**	**0.43**

*from Yde *et al.* (2014)

Table 3: Summarized values of two major ion ratios for ESL ground ice and other environmental sources. Samples with ratios < 1 are marked in bold.

The TDS in Gemini ice is low (~10 mg/l). Unlike other ESL ground ice, Gemini ice is composed of $Ca-HCO_3$ waters (Figure 6), which represent a strong terrestrial signal. The $(Na^{+}+K^{+})/Ca^{2+}$ and Cl^{-}/HCO_3^{-} ratios of G-3 ice samples are less than unity (Table 3). In fact, Gemini ice has virtually the same major ion ratios as glacial ice from the Greenland Ice Sheet (Yde et al. 2014). Interestingly, only one sub-sample from G-3 core showed an Na-Cl marine signal – ice extracted from sediment directly overlying the massive ice. This is consistent with surficial mapping which identifies sediments in the Gemini area as having a marine origin (Aitken and Bell 1998; Bell and Hodgson 2000).

There is little evidence that glacial meltwater mixed with marine waters or sediments at Gemini. The geochemical signal in the massive ice is purely glacial. Furthermore, the freezing slopes produced by co-isotope plots for G-1 and G-3 ice equal or exceed the LMWL. If the Gemini ice has a segregated origin, freezing would have had to proceed in one of two scenarios: i) very slowly, to allow for constant migration of unfrozen water to the freezing front in order to produce such massive, pure lenses (but after such slow freezing, the effects of equilibrium isotopic fractionation should be apparent in the isotopic signature of the ice, instead of “meteoric” slopes), or ii) it could have frozen quickly if there was water being supplied as quickly as it could freeze, presumably under a strong pressure gradient. The largely conformable upper contact and absence of glacial till in the exposure are still the most convincing arguments against the presence of buried ice.

5.2) Transfer of ice sheet meltwater to freezing front

The model of landscape-scale massive ice formation by the process of ice segregation proposed by Pollard et al. (2015) requires the infiltration of large volumes of subglacial meltwater into a permeable, conductive geologic unit beneath an ice sheet.

Ice sheets produce meltwater on their surface (supraglacial zone) and at their base (subglacial zone). The rate of supraglacial meltwater production is largely controlled by seasonal and local weather patterns, while rates of subglacial meltwater production are explained by friction due to ice flow and melt from water flow (Ravier and Buoncristiani 2018). Even cold-based, polar ice sheets have large areas of basal melting (Paterson 1994). According to Boulton et al. (2007), 35-45% of meltwater derived from the surface of Breidamerkurjökull (which they describe as an analogue for sediment-based Pleistocene ice sheets of North America) penetrates to the glacier bed. The modern Greenland Ice Sheet (GIS) is a better analogue for the former Innuitian Ice Sheet. It would be expected that the snow, firn and ice layers of a colder, polar ice sheet, such as the GIS, would be less permeable than the more temperate Bredamerkurjökull, making basal melting a larger source to subglacial drainage. However, recent work has emphasized the importance of *moulins*, large shaft-like openings, for transferring surface meltwater to the subglacial zone on the GIS (Gulley et al. 2009; Catania and Neumann 2010), so subglacial Innuitian meltwater may have been composed of both basal and surface melt.

In any case, when ice sheets overlie permeable materials, such as the unconsolidated Tertiary sandstones and shales of the ESL, infiltration of subglacial meltwater into the bed and into groundwater circulation is expected. In fact, some argue that beneath large ice sheets most, if not all subglacial meltwater enters the bed and flows as groundwater in the direction of the glacier terminus (e.g. Boulton and Dobbie 1993; Lemieux et al. 2008; Ravier and Buoncristiani 2018). The flow pattern of groundwater beneath the ice sheet is characterized by a net downwards flow vector due to the ice overburden pressure values. Beyond the glacial margin, there is strong upward flow due to decreasing overburden pressure (Ravier and Buoncristiani 2018). Upwelling of groundwater flow at or near the glacial margin has been reported in the field at Bredamerkurjökull by Boulton et al. (2007). In the Canadian High Arctic, upwelling of large volumes of meltwater through subglacial sediments at the glacier terminus has been observed at John Evans Glacier on eastern Ellesmere Island (Skidmore and Sharp 1999). Groundwater flow paths are affected by the hydraulic conductivity of overlying sediments and the existence of proglacial permafrost. Where proglacial permafrost exists, groundwater discharge will only occur away from the glacial margin at taliks (Ravier and Buoncristiani 2018). The fine-grained silts and clays of the ESL, a consequence of marine transgression, acted as a hydraulic aquitard as the ice margin retreated, limiting the loss of meltwater by upwelling. Rapid permafrost aggradation effectively turned the overlying sediment into an aquiclude, capping the ever-increasing ice lens growing at the aquifer-aquiclude interface. There are a number of proglacial pingos on Axel Heiberg Island which also reflect this hydrologic model (Pollard 2017).

5.3) Permafrost evolution

A transect of ground ice profiles across an elevation gradient allows us to track the evolution of Holocene permafrost aggradation in ESL sediments. Pollard and Bell's (1998) landscape model predicts that downwards freezing would have started as land first emerged at marine limit (~143 m a.s.l.). The sample sites in this study listed in chronological order of permafrost aggradation would be thus: Gemini, Black Top, Station Creek, Dump Slump (see Figure 2 for estimated dates of emergence). The nature of the ground ice at each elevation gives clues into the rate of permafrost aggradation at the time of emergence.

Climate reconstructions have revealed that starting at about 10,000 yrs BP, during the initial break-up of the Innuitian Ice Sheet, the High Arctic experienced rapid warming. Air temperatures exceeded modern values by up to 5-8°C (Lecavalier et al. 2017). It must be noted that even with an increase of 5-8°C, the mean annual air temperature at Eureka would still be in the range of -14 to -11°C, much colder than current annual air temperatures in the Low Arctic. Even in a "warmer" Arctic, subaerial freezing of recently emerged sediments would be expected to proceed quickly, as there would exist a large thermal disequilibrium between the air and ground. Early Holocene Arctic temperature reconstructions are based on proxies such as Agassiz Ice Cap $\delta^{18}O$ and pollen records, bowhead whale bones, lake sediments and peat sequences (Briner et al. 2016; Lecavalier et al. 2017). Besides a few sudden cooling episodes (e.g. the 8.2 kya event), the High Arctic remained warmer than present through the early Holocene (although still cold enough for permafrost to aggrade into recently emerged sediments). Following a period of exceptionally warm temperatures around 6-5,000 yrs BP (coinciding with the Holocene Thermal Maximum), a general cooling trend began that culminated in the Little Ice Age in 1700 AD. The current warming trend is unprecedented in at least the last 5,000 yrs (Briner et al. 2016; Lecavalier et al. 2017).

Permafrost began aggrading at the Gemini site between 8,500 and 8,000 yrs BP. Overall, this was a period of rapid warming associated with the break-up of highland ice caps. Assuming the Gemini massive ice is segregated, this would coincide with a remarkably stable freezing front to allow for the constant supply of upwelling meltwater to form pure ice at the base of the marine sediments. On the other hand, it is widely accepted that ~8,200 yrs BP there was an abrupt climate fluctuation where temperatures in central Greenland dropped by 4-8°C over ~150 years (Barber et al. 1999; Briner et al. 2016). The cause of the sudden cooling is believed to be associated with a massive outflow of fresh water from the Hudson Strait following the collapse of the northern ice dam of glacial lakes Agassiz and Ojibway (Barber et al. 1999). In many Arctic locales, this climatic event is linked with stable or re-advancing glacial margins, known as the Cockburn substage (Young et al. 2012; Briner et al. 2016). Interestingly, glacial re-advances are linked with burial of glacial ice. In any case, the rate of freezing is hard to infer based on the Gemini exposure, as it is unclear if the massive, pure ice is a reflection of a slow freezing rate or pressurized groundwater.

The Black Top (BT) slump is situated between 60-70 m a.s.l., corresponding with a period of emergence ~7-7,500 yrs BP. This corresponds with a moderate warm period – a minor lull in the warming trend following the onset of deglaciation. The BT cores contain dirty massive ice with volumetric ice contents from 50-80%. Hodgson and Nixon (1998) found similar ice content in cores taken from the same elevation range (excluding those taken from ice wedges). In general, Hodgson and

Nixon (1998) recorded pure (>95% fV_i) massive ice at lower (35-55 m a.s.l.) or higher (90-130 m a.s.l.) elevations across the ESL. It is possible that the dirtier ice found at this elevation across the ESL is due to a more rapidly advancing freezing front during the time of emergence. The migration of isotopically-depleted groundwater was limited – thus most of the water supplying the massive ice was brackish water within the marine sediments. There is no discernible difference in sediment texture between the Black Top site and the Station Creek or Dump Slump sites (silty clays coarsening with depth to silty loams).

Relative sea level curves (e.g. Simon et al. 2015) place Station Creek and Dump Slump exposures (40-50 m a.s.l.) as emerging at approximately 5,000 yrs BP. Both are examples of pure (>95% fV_i) massive ice. Their approximate time of formation coincides with a relatively warm period in the Canadian High Arctic. Air temperatures are estimated to be 3-4°C warmer than pre-industrial modern values. Downwards freezing of the ground would proceed at a slower rate under warmer air temperatures. This created a stable freezing front, allowing unfrozen groundwater (glacial melt) to migrate through the aquifer (fractured, unconsolidated Tertiary bedrock) and form massive ice at the aquifer-marine sediment interface over the span of 10^2-10^3 yrs.

6. Conclusions

The aim of this study was to confirm the origin of massive ground ice in the Eureka Sound Lowlands through field observations and permafrost core analysis (especially, stable water isotopes and major ions). The results lead to the following conclusions:

I. Massive ground ice in the Eureka Sound Lowlands formed synchronously with marine regression, as water migrated upwards to a stable freezing front near the interface of fine-grained marine sediments and an underlying, permeable geologic unit.

II. The massive ground ice formed in an open freezing system with an initial reservoir of remnant marine water within the fine-grained sediments, mixed with an input of isotopically-depleted glacial meltwater supplied by the permeable layer below.

III. Massive ground ice exposures with the highest volumetric ice contents are associated with the most isotopically-depleted ice. In these cases, the input of glacial meltwater is expected to have been much greater than the downwards freezing rate.

IV. "Apparent" meteoric co-isotope slopes can be produced in ground ice that formed in an open system with an input that has a significantly different isotopic signature than an initial reservoir.

V. The rate of permafrost aggradation into newly-emerged marine sediments was faster in the early-Holocene (~7,500 yrs BP), as indicated by lower volumetric ice contents, heavier isotopic signatures and stronger marine hydrochemical signals in massive ice at corresponding elevations. In contrast, permafrost aggradation rates are inferred to be slower during the mid-Holocene (~5,000 yrs BP) due to the presence of thick bands of "pure", isotopically-depleted massive ice at these elevations, a reflection of a slow freezing front.

7. References

Bell T (1996) The last glaciation and sea level history of Fosheim Peninsula, Ellesmere Island, Canadian High Arctic. Canadian Journal of Earth Sciences 33: 1075-1086

Bell T, Hodgson DA (2000) Quaternary geology and glacial history of Fosheim Peninsula, Ellesmere Island, Nunavut. In Garneau M, Alt B (eds.) *Environmental Response to Climate Change in the Canadian High Arctic*. Geological Survey of Canada Bulletin 529: 175-187

Coulombe S, Fortier D, Lacelle D, Kanevskiy M, Shur Y (2019) Origin, burial and preservation of late Pleistocene-age glacier ice in Arctic permafrost (Bylot Island, NU, Canada) *The Cryosphere* 13: 97-111

Couture N, Pollard WH (1998) An assessment of ground ice volume near Eureka, NWT. *Proceedings of the 7th International Conference on Permafrost* 55: 195-200

Dansgaard W (1964) Stable isotopes in precipitation. *Tellus* 16(4): 436-468

Dyke AS, Savelle JM (2000) Major end moraines of Younger Dryas age on Wollaston Peninsula, Victoria Island, Canadian Arctic: implications for paleoclimate and for formation of hummocky moraine. *Canadian Journal of Earth Sciences* 37 (4): 601-619

England J, Atkinson N, Bednarski J, Dyke AS, Hodgson DA, O Cofaigh C (2006) The Innuitian Ice Sheet: configuration, dynamics and chronology. *Quaternary Science Reviews* 25: 689-703

French HM, Harry DG (1990) Observations on buried glacier ice and massive segregated ice, western Arctic coast, Canada. *Permafrost and Periglacial Processes* 1: 31-43

Fritz M, Wetterich S, Meyer H, Schirrmeister L, Lantuit H, Pollard WH (2011) Origin and characteristics of massive ground ice on Herschel Island (Western Canadian Arctic) as revealed by stable water isotope and hydrochemical signatures. *Permafrost and Periglacial Processes* 22: 26-38

Hodgson DA (1985) The last glaciation of west-central Ellesmere Island, Arctic Archipelago. *Canadian Journal of Earth Sciences* 22: 347-368

Hodgson DA, Nixon FM (1998) Ground ice volumes determined from shallow cores from western Fosheim Peninsula, Ellesmere Island, Northwest Territories. *Geological Survey of Canada - Bulletin 507*. Natural Resources Canada: Ottawa.

IAEA/WMO (2018) Global Network of Isotopes in Precipitation. *The GNIP Database*. Accessible at http://www.iaea.org/water

Kern Z, Fórizs I, Pavuza R, Molnár M, Nagy B (2011) Isotope hydrological studies of the perennial ice deposits of Saarhalle, Mammuthöhle, Dachstein Mts, Austria. *The Cryosphere* 5: 291-298

Lecavalier BS, Fisher DA, Milne GA, Vinther BM, Tarasov L, Huybrechts P, Lacelle D, Main B, Zheng J, Bourgeois J, Dyke AS (2017) High Arctic Holocene temperature record from the

Agassiz ice cap and Greenland ice sheet evolution. *Proceedings of the National Academy of Sciences* 114: 5952-5957

Lewkowicz A (2007) Dynamics of active-layer detachment failures, Fosheim Peninsula, Ellesmere Island, Nunavut, Canada. *Permafrost and Periglacial Processes* 18: 89-103

MacKay JR (1971) The origin of massive icy beds in permafrost, western arctic coast, Canada. *Canadian Journal of Earth Sciences* 8: 397-422

Overduin PP, Westermann S, Yoshikawa K, Haberlau T, Romanovsky V, Wetterich S (2012) Geoelectric observations of the degradation of nearshore submarine permafrost at Barrow (Alaskan Beaufort Sea). *Journal of Geophysical Research: Earth Surface* 117: F02004

Pollard, W.H. (2017) Periglacial processes in glacial environments. Ch 15. In: Menzies & Japp.: Past Glacial Environments, 2nd ed. Elsevier. 585 p

Pollard, W.H., 1991. Observations on massive ground ice on Fosheim Peninsula, Ellesmere Island, Northwest Territories; In Current Research, Part E, Geological Survey of Canada, Paper 91-1E, p. 223-231.

Pollard WH (2000a) Distribution and characterization of ground ice on Fosheim Peninsula, Ellesmere Island, Nunavut. In Garneau M, Alt B (eds.) *Environmental Response to Climate Change in the Canadian High Arctic*. Geological Survey of Canada - Bulletin 529: 207-233

Pollard WH (2000b) Ground-ice aggradation on Fosheim Peninsula, Ellesmere Island, Nunavut. In Garneau M, Alt B (eds.) *Environmental Response to Climate Change in the Canadian High Arctic*. Geological Survey of Canada - Bulletin 529: 325-333

Pollard WH, Ward MK, Becker M (2015) The Eureka Sound lowlands: an ice-rich permafrost landscape in transition. *Proceedings of GeoQuebec Conference, Quebec QC* (September 20-23, 2015)

Pollard WH, French HM (1980) A first approximation of the volume of ground ice, Richards Island, Pleistocene Mackenzie delta, Northwest Territories, Canada. Canadian Geotechnical Journal 17: 509-516

Rampton VN (1988) *Quaternary geology of the Tuktoyaktuk Coastlands, Northwest Territories*. Geological Survey of Canada: Memoir 423

Robinson, S. & Pollard, W. (1998). Massive ground ice within Eureka Sound bedrock, Fosheim Peninsula, Ellesmere Island, NWT. *Proceedings, Seventh International Permafrost Conference*, edited by A.G. Lewkowicz, and M. Allard, Yellowknife, 23 27 June, Université Laval, Centre d' études nordiques, Collection Nordicana, No 57, 949 954.

Simon K, Dyke A, James TS (2015) A new glacial isostatic adjustment model of the Innuitian Ice Sheet, Arctic Canada. *Quaternary Science Reviews* 119: 11-21

Souchez RA, Jouzel J (1984) On the isotopic composition in $\delta^{18}O$ of water and ice during freezing. *Journal of Glaciology* 30: 369-372

Souchez RA, JM de Groote (1985) δD-$\delta^{18}O$ relationships in ice formed by subglacial freezing: paleoclimatic implications. *Journal of Glaciology* 31: 229-232

Stendel M, Rodehacke C, Romanovsky V, Nicolski D, Marchenko S, Christensen JH, Mottram R, Oleson M (2016) How permanent is East Siberian Arctic Shelf permafrost? *Proceedings of the XI International Conference on Permafrost*, Gunther F, Morgenstern A (eds.), Potsdam, Germany: 81

Steven B, Pollard WH, Greer CW, Whyte LG (2008) Microbial diversity and activity through a permafrost/ground ice core profile from the Canadian High Arctic. *Environmental Microbiology* 12: 3388-3403

Vaikmae R, Michel FA, Solomatin VI (1993) Morphology, stratigraphy and oxygen isotope composition of fossil glacier ice at Ledyanaya Gora, Northwest Siberia, Russia. *Boreas* 22: 205-213

Ward Jones MK, Pollard WH, Jones B (2019) Rapid initialization of retrogressive thaw slumps in the Canadian high Arctic and their response to climate and terrain factors. *Environmental Research Letters* 14: 055006

Yde JC, Knudsen NT, Hasholt B, Mikkelsen AB (2014) Meltwater chemistry and solute export from a Greenland Ice Sheet catchment, Watson River, West Greenland. *Journal of Hydrology* 519(B): 2165-2179

Additional Figures

1. Na-Cl
"Marine"

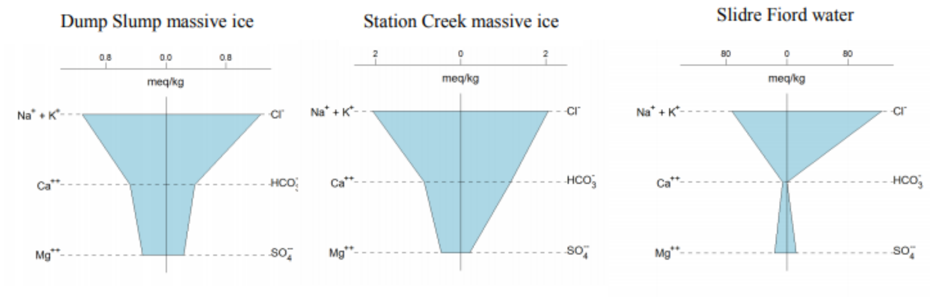

2. Na-HCO3
"Leachate"

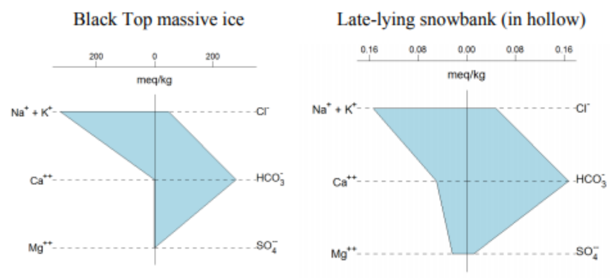

3. Ca-HCO3
"Terrestrial/Glacial"

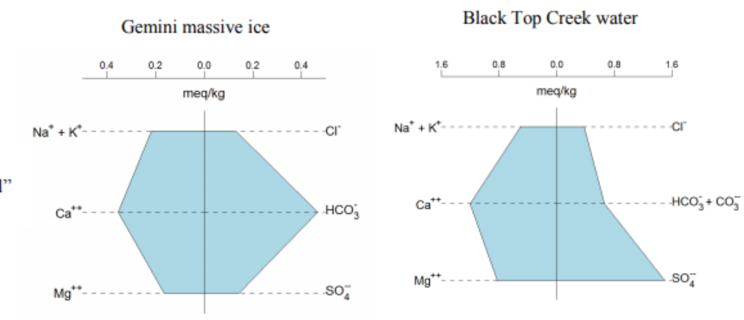

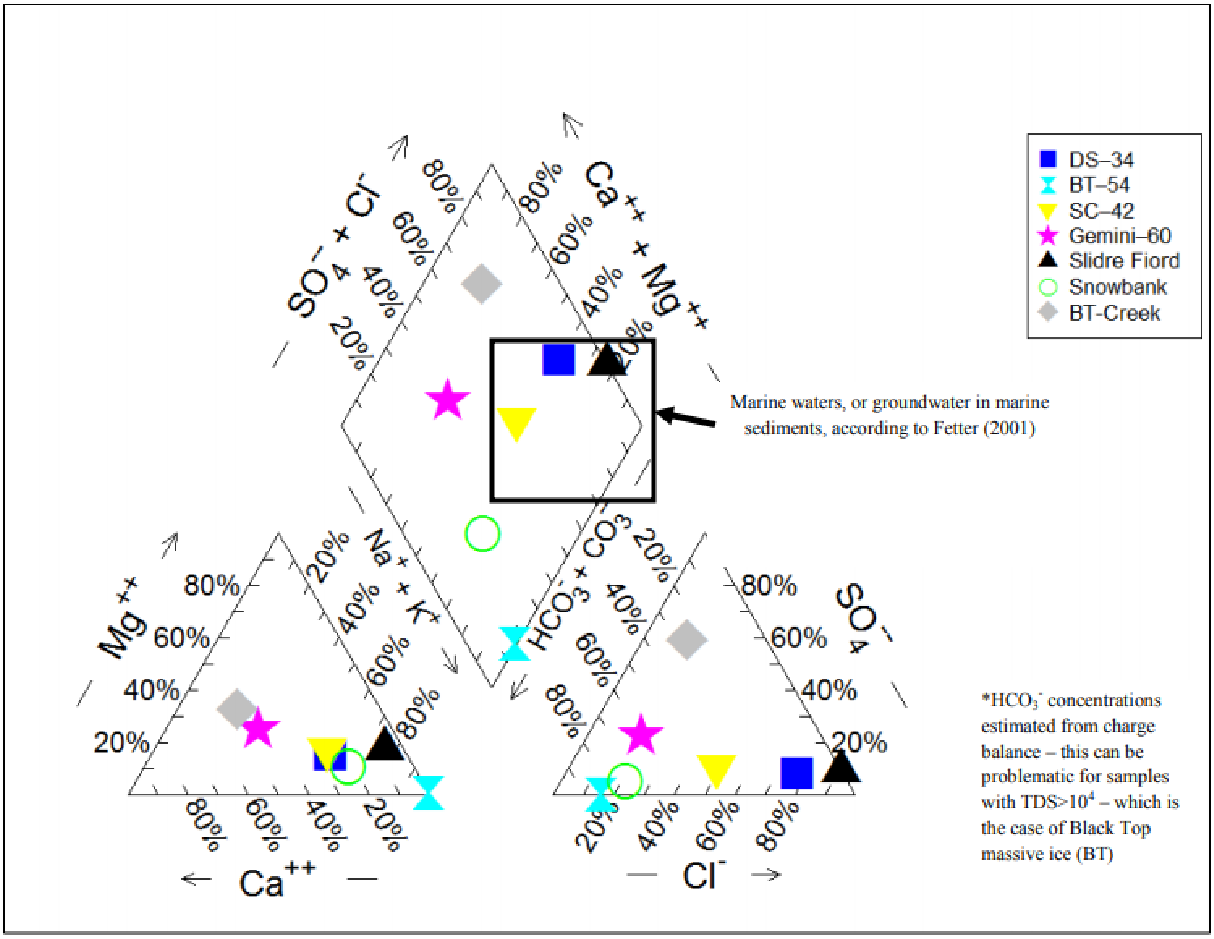
DS–34
BT–54
SC–42
Gemini–60
Slidre Fiord
Snowbank
BT-Creek
Marine waters, or groundwater in marine sediments, according to Fetter (2001)
SO4 + Cl
Ca++ + Mg++
Na+ + K+
HCO3 + CO3
Mg++
Ca++
SO4
Cl
80%
60%
40%
20%
*HCO3 concentrations estimated from charge balance – this can be problematic for samples with TDS>10⁴ – which is the case of Black Top massive ice (BT)

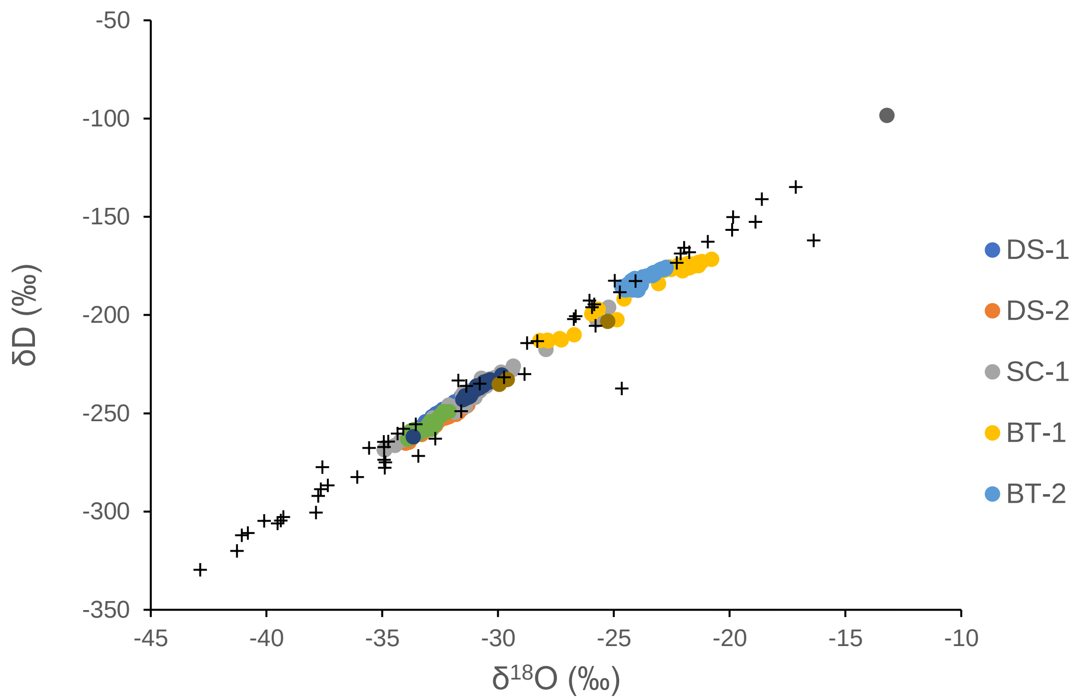

-50
-100
-150
-200
-250
-300
-350
-45
-40
-35
-30
-25
-20
-15
-10
δD (‰)
δ18O (‰)
DS-1
DS-2
SC-1
BT-1
BT-2